

A claudin5-binding peptide enhances the permeability of the blood-brain barrier in vitro

Martina Trevisani^{1,2†}, Alessandro Berselli^{1,3†}, Giulio Alberini^{1,3*}, Eleonora Centonze¹, Silvia Vercellino^{1,3}, Veronica Cartocci^{1,3}, Enrico Millo², Dinu Zinovie Ciobanu⁴, Clarissa Braccia⁴, Andrea Armirotti⁴, Francesco Pisani^{1,5}, Federico Zara^{6,7}, Valentina Castagnola^{1,3*†}, Luca Maragliano^{1,8†}, Fabio Benfenati^{1,3†}

The blood-brain barrier (BBB) maintains brain homeostasis but also prevents most drugs from entering the brain. No paracellular diffusion of solutes is allowed because of tight junctions that are made impermeable by the expression of claudin5 (CLDN5) by brain endothelial cells. The possibility of regulating the BBB permeability in a transient and reversible fashion is in strong demand for the pharmacological treatment of brain diseases. Here, we designed and tested short BBB-active peptides, derived from the CLDN5 extracellular domains and the CLDN5-binding domain of *Clostridium perfringens* enterotoxin, using a robust workflow of structural modeling and *in vitro* validation techniques. Computational analysis at the atom level based on solubility and affinity to CLDN5 identified a CLDN5-derived peptide not reported previously called f1-C5C2, which was soluble in biological media, displayed efficient binding to CLDN5, and transiently increased BBB permeability. The peptidomimetic strategy described here may have potential applications in the pharmacological treatment of brain diseases.

Copyright © 2025 The Authors, some rights reserved; exclusive licensee American Association for the Advancement of Science. No claim to original U.S. Government Works. Distributed under a Creative Commons Attribution NonCommercial License 4.0 (CC BY-NC).

INTRODUCTION

The blood-brain barrier (BBB) represents the primary defense layer for the brain and has a pivotal role in maintaining its homeostasis. However, it also hinders therapeutic interventions in case of brain disorders, such as neurodegeneration, glioblastoma, and various genetic diseases (1, 2). As a notable example, in the glucose transporter-1 deficiency syndrome (GLUT1DS) a loss-of-function mutation in the *SLC2A1* gene encoding for the unique Glut1 transporter in brain endothelial cells prevents the appropriate supply of glucose to maintain physiological brain functions (3–5).

Because of these limitations, there is a high demand for innovative approaches to regulate BBB permeability under pathological conditions (1, 6–10). Many strategies are under investigation to increase the passage of small molecules across the BBB, by facilitating either their crossing of the endothelial cells (the transcellular route) or their passage between adjacent endothelial cells (the paracellular route) (6, 11–18). The BBB paracellular pathway is controlled by specialized protein assemblies called tight junctions (TJs), whose backbone is formed by members of the claudin (CLDN) family (19, 20). These proteins comprise a four-transmembrane helix bundle (TM1–4) with two extracellular loops (ECL1–2), cytoplasmic N/C termini, and an intracellular loop (19–22). To form TJs, CLDN monomers polymerize in strands within the lateral membrane of endothelial cells, while strands from neighboring cells

associate across the paracellular space. CLDN5 is the most expressed member of the family in the TJs of the BBB and has a key role in restricting the paracellular traffic of molecules and ions (1, 22). Since no experimental studies have shed light on the structure of TJ assemblies of CLDNs so far, the current knowledge of their multimeric organization relies only on computational modeling (19, 23–25). Many studies suggest that the interactions between the CLDN ECL domains along the TJ strands result in porous scaffolds that partially occlude the paracellular space (20, 23, 26). Many works demonstrated that these pores convey the paracellular fluxes and act as a selectivity filter for ion-permeable CLDNs (24, 27–31). However, in previous studies, ours and another group showed that these architectures are also consistent with the physiological function of barrier-forming CLDNs since, when they are assembled with CLDN5 monomers, they are not permissive to ions (24, 25, 32). For this reason, hereafter we use the word “pore” (intended as a structural feature) when discussing cavity-forming assemblies for the barrier-forming CLDN5.

Inspired by studies on CLDN1- (14, 33) and CLDN4- (34, 35) expressing cells, efforts have been recently devoted to design molecular approaches based on competing peptides able to modulate the formation of CLDN5 multimers. Two families of peptides have been investigated, including (i) derivatives of the nontoxic C-terminal domain of *Clostridium perfringens* enterotoxin (cCPE) (12, 36, 37) and (ii) a peptidomimetic based on the murine CLDN5 (mCLDN5) ECL1 domain, known as C5C2 (11, 37). Despite these seminal endeavors, the design of CLDN-modulating peptides has been hindered by the limited structural information available on these proteins. Although the structure of other CLDNs in the monomeric form has been determined experimentally (38–41), that of CLDN5 is not yet available. Moreover, there are still major gaps in our understanding of the assembly of CLDNs in TJs, and the only detailed structural models currently available originate from computational approaches (19, 23–25). In addition, the length of the CLDN5-modulating peptides identified so far (30 amino acids for C5C2 and up to 170 amino acids for the modified cCPE) presents difficulties for both experimental and computational methods to

¹Center for Synaptic Neuroscience and Technology (NSYN@UniGe), Istituto Italiano di Tecnologia, Largo Rosanna Benzi, 10, 16132 Genova, Italy. ²Department of Experimental Medicine, Università degli Studi di Genova, Viale Benedetto XV, 3, 16132 Genova, Italy. ³IRCCS Ospedale Policlinico San Martino, Largo Rosanna Benzi, 10, 16132 Genova, Italy. ⁴Analytical Chemistry Facility, Istituto Italiano di Tecnologia, Via Morego 30, 16163 Genova, Italy. ⁵Department of Biosciences, Biotechnologies and Biopharmaceutics, University of Bari “Aldo Moro”, 70125 Bari, Italy. ⁶Department of Neurosciences, Rehabilitation, Ophthalmology, Genetics, Maternal and Child Health (DINO/MI), University of Genova, 16132 Genova, Italy. ⁷Medical Genetics Unit, IRCCS Giannina Gaslini Institute, 16147 Genova, Italy. ⁸Department of Life and Environmental Sciences, Polytechnic University of Marche, Via Brecce Bianche, 60131 Ancona, Italy.

*Corresponding author. Email: giulio.alberini@iit.it (G.A.); valentina.castagnola@iit.it (V.C.)

†These authors contributed equally to this work.

study protein-peptide interactions, not to speak about their potential translatability to the clinics. While computational techniques can be crucial to understanding the atomic details of the binding process, they are usually limited to peptides not exceeding 15 residues (42–47), with at least one remarkable and very recent exception (48). As for the experimental side, shorter sequences are beneficial in terms of synthesis, solubility, conformational stability, and translatability (49).

In this work, we investigate a group of peptidomimetics designed in house and extracted from either C5C2 or cCPE, characterized by a short chain length (<20 amino acids). Our study is based on a multidisciplinary approach, integrating computational methods and *in vitro* BBB models. Leveraging this workflow to screen a set of designed peptides, we identified an original 14-mer peptide [named f1-C5C2, sequence ESQLALNAEVQAAR, corresponding to the mCLDN5 fragment comprising the residues 68 to 81 and including the previously reported S74N substitution (11)] that exhibits affinity for CLDN5. This peptide, assayed in two-dimensional (2D) murine *in vitro* models of the BBB, transiently and reversibly increases the paracellular permeability at relatively low concentrations and short incubation times. The multidisciplinary workflow described here can provide hints to design selective enhancers of drug/molecule delivery across biological barriers and CLDN-based paracellular complexes.

RESULTS

Design of short CLDN5-binding peptides

To predict whether the mCLDN5 peptidomimetics could compete with the interactions that stabilize the paracellular TJ scaffold, we visualized CLDN5 assemblies using structural models. Although there is no experimental structure available for CLDN-based TJ complexes, several models have been proposed (26). Here, we used two CLDN5 multi-pore architectures, one based on the template previously published for the homolog mCLDN15 (26) (Fig. 1, A to C) and the other on the back-to-back interaction interface introduced for CLDN5 (Fig. 1, D to F) (23). Consistent with our previous work (25, 32), these models were built using the human CLDN5 (hCLDN5) protomer. However, we emphasize that the sequence identity between the human (UNIPROT: O00501) and the murine (UNIPROT: O54942) CLDN5 sequences is ~92%, as shown by the sequence alignment performed with Clustal Omega (50, 51) and reported in fig. S1A. For this reason, the multi-pore configurations assembled using either hCLDN5 or mCLDN5 should not differ in this context.

Short peptides that could potentially bind CLDN5 were identified starting from sequences previously used to target this protein [C5C2 (11) and cCPE (12)]. These peptides, composed of more than 30 amino acids, were fragmented into shorter chains, with a maximal length of 16 residues. For the cCPE-derived ones, the domains responsible for the association with CLDN5 were considered (12). In both human and murine architectures, the sequence of the first selected peptide, f1-C5C2, coincides with the region of the CLDN5 ECL1 domain responsible for the formation of both hydrophobic cis- and trans-interactions with adjacent and facing CLDN subunits, respectively (Fig. 1, B and E). Specifically, the f1-C5C2 fragment represents the extracellular helix domain of CLDN5 protomers and includes the residue V70 (corresponding to M68 in mCLDN15) that stabilizes the so-called cis-linear interface (26) with the hydrophobic residues F147, Y148, and L160 (F146, F147, and L158 in mCLDN15) belonging to

the adjacent monomer (Fig. 1, C and F). Furthermore, this segment participates in multiple trans-interactions involving the apolar contact between L71 of one monomer's ECL1, P153, and V154 on the facing monomer's ECL2 (fig. S1, B and C). The second C5C2-based fragment, f2-C5C2, differs from f1-C5C2 for the absence of the glutamate and the serine at the N terminus, hence affecting its solubility in water.

cCPE-derived peptides were defined leveraging a model of the hCLDN5-cCPE complex. To assemble this system, a homology-based hCLDN5 protomer was aligned with the hCLDN4 crystal structure, which was solved bound to the bacterial toxin [Protein Data Bank (PDB) ID: 5B2G (39)]. In addition, because CLDN5 is not a biological target for cCPE, the ligand was modified as suggested previously (12). In the resulting hCLDN5-cCPE model (Fig. 1G), three fragments (f1-cCPE, f2-cCPE, and f3-cCPE, Fig. 1, H and I) with a length between 11 and 16 residues were selected from the binding interface. Thereafter, single-point mutations were introduced in the f1-C5C2, f1-cCPE, f2-cCPE, and f3-cCPE sequences to improve their solubility in water, generating the peptide data bank reported in table S1.

In silico and experimental assessment of peptide solubility

To predict the solubility of the peptide data bank that encompasses both cCPE and C5C2-derived fragments, we performed all-atom molecular dynamics (MD) simulations of multiple copies of each species in water and a KCl/CaCl₂ ionic bath mimicking the ionic strength of the Dulbecco's modified Eagle's medium (DMEM) used in cell cultures. To properly classify each peptide, we designed a machine learning approach (fig. S2) based on three solubility descriptors calculated along the simulations: the number of peptides' aggregates, the size of the largest aggregate, and the number of their contacts with water molecules (see section S1). The method was trained on an external dataset of peptides of known solubility and allowed us to classify all our sequences into two neatly distinct families (see tables S1 and S2 for test and train sets, respectively, and fig. S3A). We discuss here the results of the representative subgroup of peptides f1-C5C2 and f3-cCPE-mut1, assigned to the soluble group, and f2-C5C2, included among the insoluble ones (fig. S3B). The presence of both soluble (f1-C5C2 and f3-cCPE-mut1) and insoluble (f2-C5C2) molecules allowed us to assess the accuracy of the solubility prediction.

The starting and final configurations from MD simulations of each of the three peptides are shown in Fig. 2 (A and B, D and E, and G and H), while additional intermediate states along the trajectories are reported in fig. S4. During the last 10 ns of the simulation, we observed that the soluble f1-C5C2 and f3-cCPE-mut1 peptides form only a few aggregates with an average size of up to ~7 and ~10 subunits, respectively (~30 and ~37% of the number of initial copies for f1-C5C2 and f3-cCPE-mut1, respectively). In addition, these peptides were appropriately dispersed in the solvent, as demonstrated by the presence of ~11 different aggregates at the end of the simulation for both systems (table S1). As for the extent of solvation, f1-C5C2 and f3-cCPE-mut1 maintained more than 75% contact with water molecules after 100 ns of MD simulation. On the contrary, f2-C5C2 formed a cluster of 12 subunits, about 45% of the total copies, and only four large aggregates were found at the end of the simulation, suggesting a marked propensity of the peptides to interact with each other rather than being individually solvated. At the end of the simulation, the number of contacts with water molecules for f2-C5C2 was ~65% of the initial value. This suggests that the surface exposed to the solvent for the system assembled with f2-C5C2 is largely lower than those of f1-C5C2

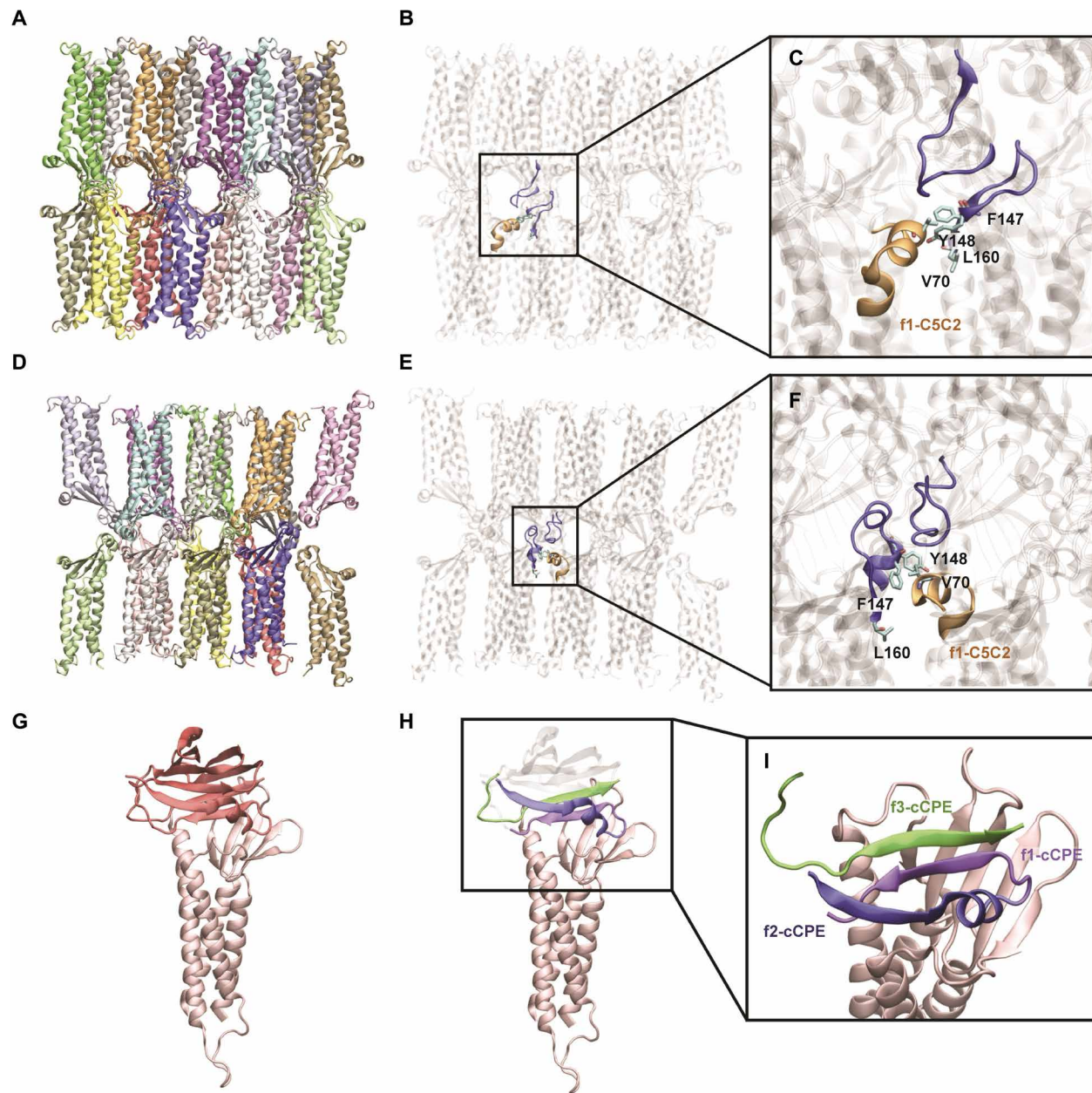


Fig. 1. Selection of CLDN5- and cCPE-based peptides from structural models. (A) Triple pore arrangement formed by multiple hCLDN5 monomers based on the mCLDN15 template (26). Individual monomers are distinguished by color. (B) The same structure as (A), with the f1-C5C2 fragment and the ECL2 segments shown in orange and blue, respectively. (C) Close-up view of the V70, F147, Y148, and L160 residues forming the cis-linear interface. The ECL2 of the monomer belonging to the opposite hCLDN5 strand is also shown. (D) Triple pore arrangement formed by multiple hCLDN5 monomers based on the CLDN-CLDN interface described in (23). Individual monomers are distinguished by color. (E) The same structure as in (D), with the f1-C5C2 fragment and the ECL2 segments shown in orange and blue, respectively. (F) Close-up view of the V70, F147, Y148, and L160 residues forming the cis-linear interface. The ECL2 of the monomer belonging to the opposite hCLDN5 strand is also shown. (G) hCLDN5-cCPE complex model generated with the modified version of the toxin (12) and aligned to the hCLDN4-cCPE crystal structure (PDB ID:5B2G). (H) The same structure as in (G), in which the binding interfaces between hCLDN5 and cCPE are highlighted. (I) Close-up view of the hCLDN5-cCPE contact domain, in which the cCPE fragments f1-cCPE, f2-cCPE, and f3-cCPE are colored in purple, blue, and green, respectively.

and f3-cCPE-mut1. In conclusion, the simulations performed in a DMEM-like ion/water solution predict a peptide solubility order f2-C5C2 < f1-C5C2 < f3-cCPE-mut1. The solubility of the three sequences was then assessed experimentally by liquid chromatography–mass spectrometry (LC-MS; Fig. 2, C, F, and I). Starting from a stock solution in H₂O/acetonitrile (ACN) 1:1 (as detailed in Materials

and Methods), each peptide sample was diluted in either Milli-Q water or DMEM until a concentration of 25 μM to assess the effect of ionic strength and pH used in the in vitro testing on the solubility. Only for f3-cCPE-mut1 the target concentration was recovered. f1-C5C2 was found in a lower concentration (about 15 μM, 60% of target concentration), but no significant solubility differences between

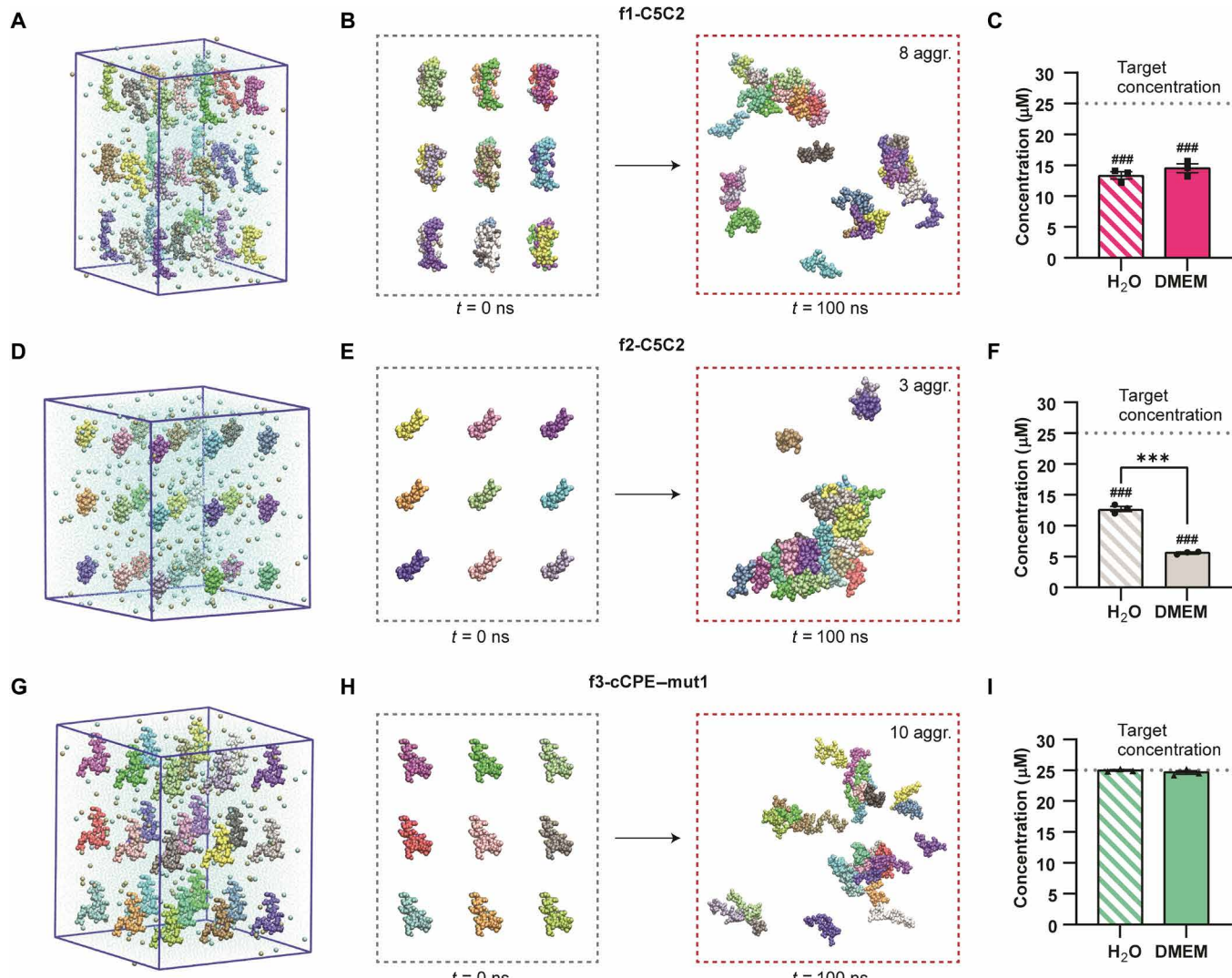


Fig. 2. Computational and experimental assessment of the peptide water solubility. (A, D, and G) Simulation boxes containing 27 identical peptides arranged in a 3D grid, solvated with water, and a mixed KCl/CaCl₂ ionic bath for f1-C5C2 (A), f2-C5C2 (D), and f3-cCPE-mut1 (G). The volume of each box fits the size of the specific peptide. (B, E, and H) Peptide configurations at the beginning (gray squares) and at the end (orange squares) of the MD simulations for f1-C5C2 (B), f2-C5C2 (E), and f3-cCPE-mut1 (H). The number of aggregates formed at the final step is indicated. (C, F, and I) Experimentally determined peptide solubility measured by LC-MS for f1-C5C2 (C), f2-C5C2 (F), and f3-cCPE-mut1 (I). For LC-MS experiments, stock solutions were diluted in H_2O and culture medium (DMEM) to a final target concentration of 25 μM (working concentration in vitro). The graphs report the absolute concentration experimentally measured by LC-MS analysis. Data are presented as means \pm SEM ($n = 3$ independent experiments with $n = 5$ technical replicates). ###P < 0.001 one-tailed Student's *t* test versus target concentration; ***P < 0.001 two-tailed Student's *t* test DMEM versus H_2O .

water and DMEM were observed. On the opposite, f2-C5C2, already found in a lower concentration in water, showed a significantly reduced value in DMEM (about 5 μM , 20% of initial target concentration), and was defined as insoluble. Hence, the solubility order in DMEM fully matches the computational predictions in the DMEM-mimicking solution.

Standard MD simulations assess the stability of mCLDN5-peptide complexes

After the solubility assessment, we proceeded with studying the binding of f1-C5C2 and f3-cCPE-mut1 to mCLDN5. We first modeled the peptide-protein complexes by performing molecular docking calculations where the flexibility of the peptides was taken into

account using an iterative procedure to scan all torsion angles (52–54). Then, the resulting docked conformations were subjected to 200 ns of standard, all-atom MD simulations, restricting the volume accessible to the peptide within the cylindrical domain shown in fig. S5. The trajectories can be visualized in the movie S1.

For mCLDN5-f1-C5C2, we observed that the complex maintains a bound state, although with a remarkable rearrangement of the peptide, which moves toward the mCLDN5 ECL1 domain (Fig. 3A). On the contrary, the mCLDN5-f3-cCPE-mut complex dissociates over the same timescale (Fig. 3B), with the peptide diffusing toward the solvent. Hence, these preliminary simulations already suggest a different affinity of the two peptides for mCLDN5.

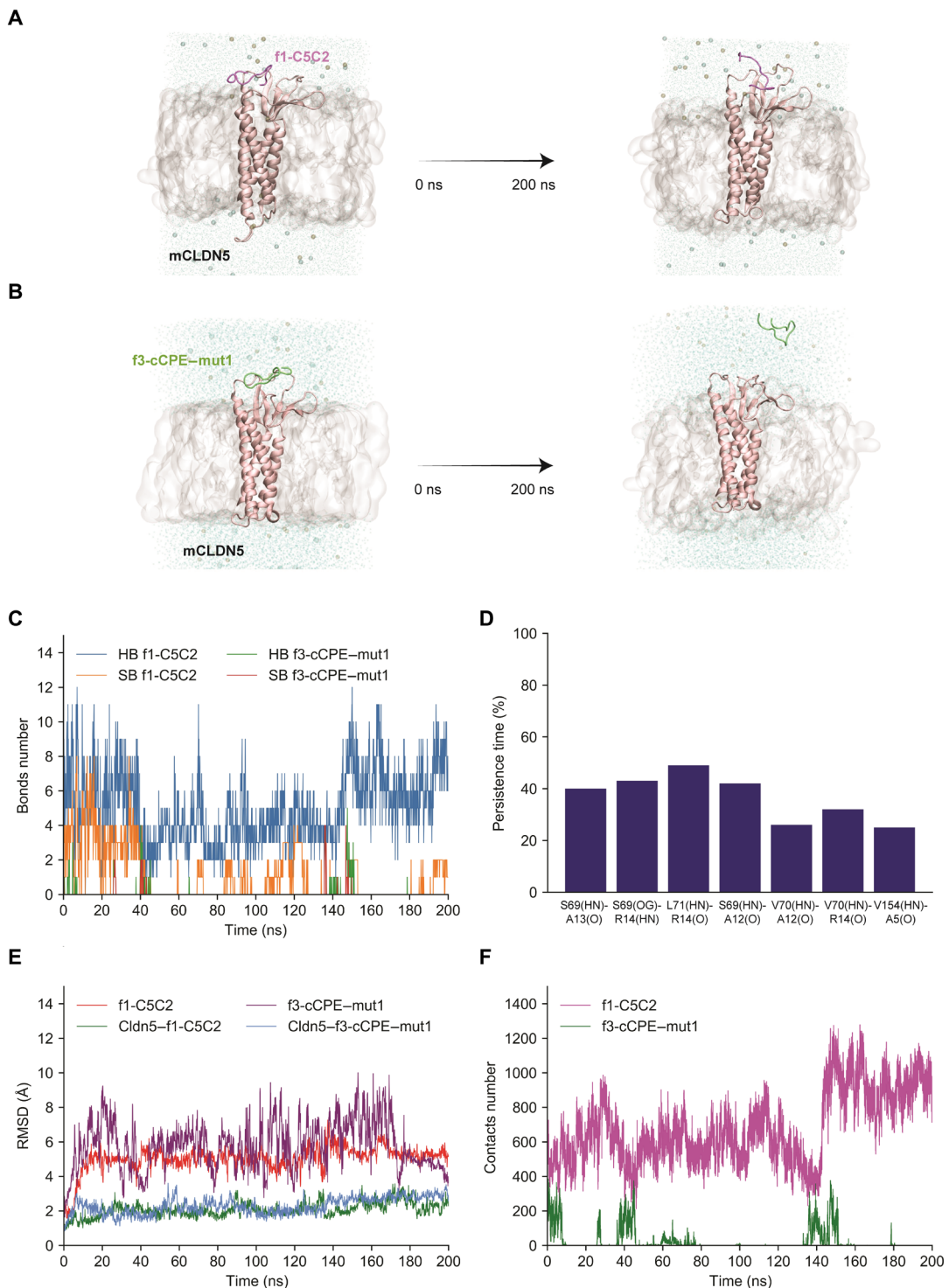


Fig. 3. Standard MD simulations of mCLDN5-peptide complexes. (A and B) Initial and final snapshots of the simulated trajectories of mCLDN5-f1-C5C2 (A) and mCLDN5-f3-cCPE-mut1 (B) complexes surrounded by the membrane bilayer (gray solid surface), water molecules (cyan points), and KCl ionic bath (blue and yellow transparent Van der Waals spheres for K^+ and Cl^- , respectively). mCLDN5 is shown with a pink cartoon representation. The f1-C5C2 and f3-cCPE-mut1 peptides are indicated as blue and green unfolded coils, respectively. (C) Number of HBs and SBs formed between the peptide and the mCLDN5 ECL domain for f1-C5C2 and f3-cCPE-mut1. (D) HBs with a persistence time > 20% of the total simulated time for f1-C5C2 are shown as blue bars. No HBs with a persistence >20% of the total simulated time were found for f3-cCPE-mut1. (E) Backbone RMSD of the peptide and the mCLDN5 ECL domain. (F) Contact number between the mCLDN5 ECL and the peptide during the MD simulation.

For both systems, we calculated the time evolution of the number of hydrogen bonds (HBs) and salt bridges (SBs) between protein and peptides, the HB persistence time, the root mean square deviation (RMSD) of the peptide, the RMSD of the mCLDN5 ECL domain, and the contact number between the protein and the peptide. The changes in the number of HBs/SBs in the mCLDN5–f1-C5C2 and mCLDN5–f3-cCPE-mut1 complexes (Fig. 3, C and D) quantify the different interactions of the two ligands with mCLDN5: While f1-C5C2 formed various HB with a persistence time >20% (Fig. 3D) involving residues S69, V70, L71, and V154 of mCLDN5 (fig. S6), no persistent interactions were found for f3-cCPE-mut1. The RMSD values of the mCLDN5 ECL domain remained stable during the MD simulations of both systems (green and cyan plots; Fig. 3E), while the RMSDs of the peptide backbone were subjected to remarkable modifications. At about ~20 ns, f1-C5C2 switched to a novel stable configuration with an RMSD of ~5 Å (red plot; Fig. 3E), while the f3-cCPE-mut1 conformation was greatly changing, with the RMSD reaching up to ~9 Å (purple plot; Fig. 3E), as a result of the increasing exposure to the solvent. Last, the number of contacts between the protein and f1-C5C2 rose up to ~1100, while the same quantity was negligible in the case of the second system (Fig. 3F).

FE calculations reveal the binding mechanism between f1-C5C2 and mCLDN5

We used the temperature-accelerated MD (TAMD) approach (55, 56) to study the unbinding of the two peptides with good solubility in DMEM, namely f1-C5C2 and f3-cCPE-mut1 from mCLDN5, using the distance between the centers of mass (COMs) of the mCLDN5 ECL domain and of the peptide as a collective variable (CV). The free energy (FE) profiles of each protein-peptide complex are shown in Fig. 4A. The curve for f1-C5C2 is characterized by a minimum of ~−6 kcal/mol at the COM-COM distance of ~10.3 Å. Beyond this distance, the FE increases until it reaches a plateau around 17.0 Å, stabilizing at the value of 0 kcal/mol, corresponding to the peptide in the bulk solvent. Using the FE profile of the complex and the formalism described in section S10, we estimate an equilibrium dissociation constant (K_d) between mCLDN5 and f1-C5C2 of 57.9 μM. On the contrary, the f3-cCPE-mut1 FE profile shows a high-energy barrier with a maximum value of ~9 kcal/mol at the smallest COM-COM distance sampled (8 Å). As the distance increases, the FE gradually decreases up to a distance of ~17 Å, where it reaches the value of 0 kcal/mol that is maintained with minimal fluctuations up to the COM-COM distance of 30.0 Å. Together, these results confirm the binding of f1-C5C2 to mCLDN5 and the repulsive interaction of the cCPE-derived peptide with the same protein. As a validation test, we repeated the FE calculations using the extended-system adaptive biasing force (eABF) method (57) and obtained very similar results (see section S2 and fig. S7). A comparative analysis of the convergence rates of the two approaches is reported in fig. S8.

The enhanced simulations allowed us to improve the sampling of the mCLDN5–f1-C5C2 poses with respect to molecular docking and standard MD simulations (whose resulting conformations are shown in Fig. 4 (B and C, respectively)). From an RMSD-based clustering of the TAMD runs, we obtained six representative structures (Fig. 4, D to I) that we analyzed for residue-residue interactions between mCLDN5 and the peptide (table S3). Most of the contacts involve residues E68, S69, V70, and L71 of ECL1, and T151, P153, V154, and Y158 of ECL2, which belong to the protein-protein contact interfaces stabilizing the hCLDN5 triple-pore models (see Fig. 1

and fig. S1). The same analysis was performed on the eABF trajectories, obtaining very similar interaction networks, as shown in fig. S7 (D to I).

In particular, it can be observed that the first three representative structures obtained from TAMD (Fig. 4, D to F) and eABF (fig. S7, D to F) simulations closely resemble the conformation of f1-C5C2 at the end of the standard MD simulation. The analysis of the interactions reported in table S3 indicates that the peptide establishes interactions with both mCLDN5 ECL1 and ECL2 domains. The SB between the f1-C5C2 E9 carboxylic side chain and the CLDN5 K48 amine group is conserved among the aforementioned structures and characterized by similar distances (~2.6 Å). Moreover, the HBs established by the f1-C5C2 A12 and R14 backbones with the mCLDN5 S69 and V70 backbones are preserved in all structures. These latter contacts are also present in the standard MD trajectories (fig. S6) for 40 to 50% of the total simulation time. Concerning the ECL2, we observe the presence of the HB interaction formed by the CLDN5 V154 and the f1-C5C2 A5 backbones and that formed between the mCLDN5 Y158 hydroxyl side chain and the f1-C5C2 E9 carboxylic group. V70 is crucial for the stabilization of the cis-linear interactions in the CLDN5 multimeric strands, whereas V154 participates in the formation of trans-interactions in the hCLDN5 multi-pore models (fig. S1, B and C). Last, this analysis reveals that the residues E1 and S2 (according to the f1-C5C2 numbering) form either few (E1) or zero (S2) contacts with mCLDN5, implying that they are important for the peptide's solubilization but not for its binding to mCLDN5.

The f1-C5C2 peptide binds CLDN5 with micromolar affinity

The binding affinity of f1-C5C2 and f3-cCPE-mut1 for mCLDN5 was estimated using microscale thermophoresis (MST) (58, 59), which allows calculating the K_d of a binding reaction by measuring variations in protein fluorescence intensity caused by a ligand (peptide) binding through a laser-induced microscopic temperature gradient. To obtain fluorescently labeled mCLDN5 while maintaining the structural integrity of the transmembrane complex, we transfected human embryonic kidney (HEK) 293T cells that do not express CLDN5 endogenously (60) with a turbo green fluorescent protein (tGFP)-tagged mCLDN5 construct (Fig. 5A). We then used cell lysates for the following MST measurements (see fig. S9). On average, green fluorescent protein (GFP, and, therefore, mCLDN5) represented 1 of 250 of the total protein content, as estimated by the fluorescence titration shown in fig. S10.

To determine the K_d of peptide binding, HEK-293T lysates containing GFP-mCLDN5 (1 μM) were incubated in MST capillaries with increasing concentrations of soluble f1-C5C2 and f3-cCPE-mut1 peptides. From the analysis shown in Fig. 5B, the resulting K_d of f1-C5C2 was ~68 μM, in excellent agreement with the value estimated from TAMD simulations (~58 μM), while experiments with f3-cCPE-mut1 and control did not display measurable binding affinity. These results fully confirmed the different peptides' selectivity for mCLDN5 proteins obtained from the FE calculations.

The f1-C5C2 peptide opens the paracellular spaces in brain endothelial cells

We then moved to investigate the functional effects of the selected peptides on an *in vitro* murine 2D Transwell model of BBB. The model was validated by monitoring the trans-endothelial electrical resistance (TEER) of the cell layer and the expression of mCLDN5, as shown in

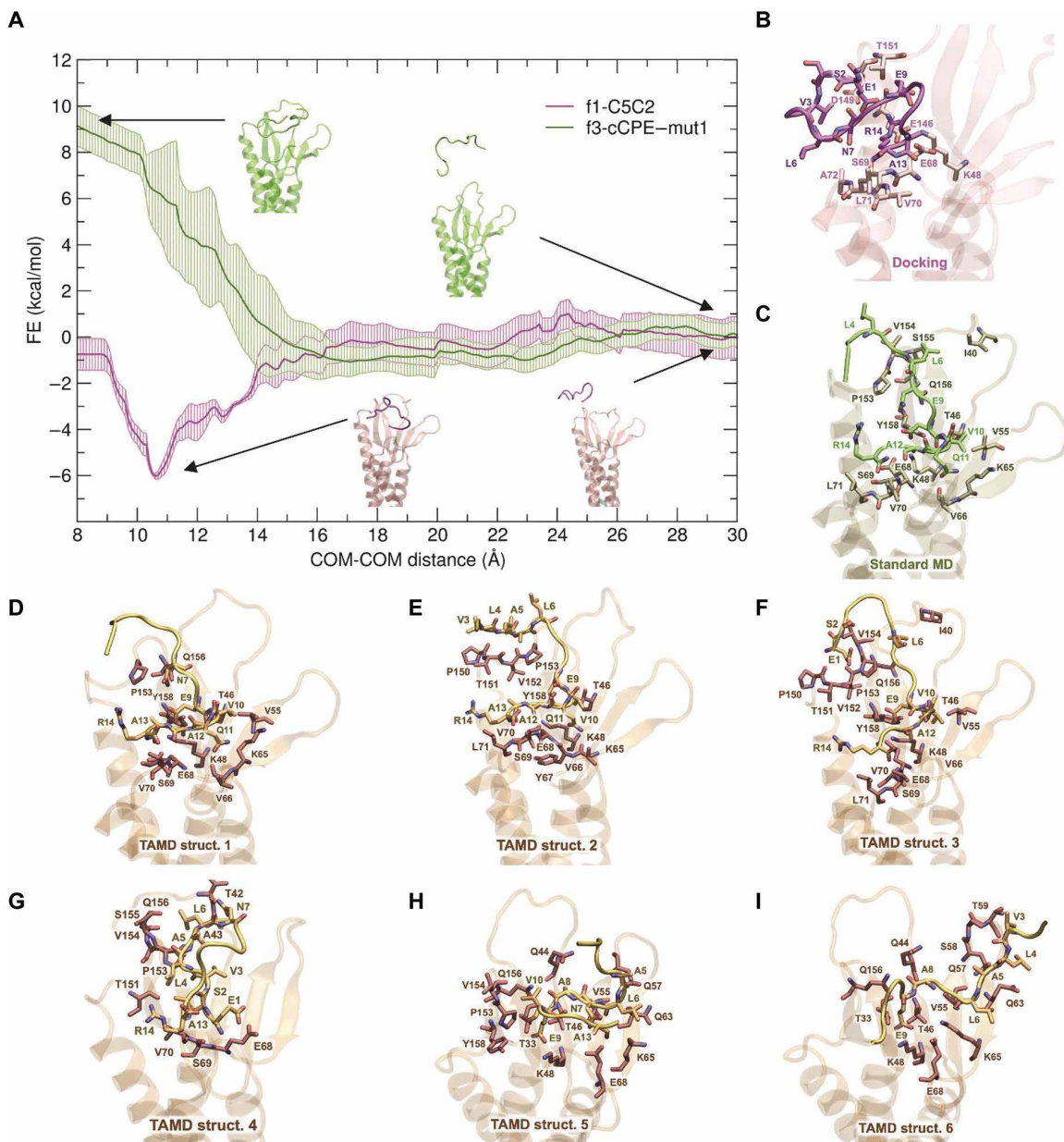


Fig. 4. mCLDN5-peptide unbinding FE calculations using TAMD. (A) FE profiles for f1-C5C2 (magenta) and f3-cCPE-mut1 (green) are computed with respect to the mCLDN5-peptide COM-COM distance with the TAMD algorithm. FE values and errors are indicated as the means and SD from three 150-ns-long replicates. Representative structures of the CLDN5-peptide complex are shown and colored in magenta and green for f1-C5C2 and f3-cCPE-mut1, respectively. (B to I) Representative mCLDN5–f1-C5C2 binding configurations provided by docking, standard MD, and clustering of TAMD trajectories. Amino acids involved in the interactions are shown as sticks and listed in table S3.

our previous work (61) and in fig. S11. All experiments were performed when the TEER values reached a plateau, indicating the correct formation of the TJs and the integrity of the endothelial barrier. The selected peptides, at the working concentration of 25 μ M, did not produce a significant change in cell viability, as assessed using a live/dead assay (fig. S12), although some morphological change in the presence of f1-C5C2 could be observed. We then monitored the changes in TEER values upon continuous incubation (c.i.) with 25 μ M of either soluble peptides f1-C5C2 or f3-cCPE-mut1 up to 72 hours (Fig. 6, A to C). We observed an immediate and progressive TEER decrease for cells incubated with

f1-C5C2, becoming highly significant after 8 hours of treatment. The decrease in TEER values (around 40% of the baseline) can be considered a proxy for the partial opening of paracellular spaces. On the contrary, TEER values remained constant when f3-cCPE-mut1 was used, in line with the results obtained for FE calculation and binding affinity. The working concentration was established from the preliminary solubility assessment by LC-MS (see Fig. 2) and is among the lowest concentrations used for CLDN5-derived synthetic peptides (11, 14), although a lower concentration was reported for a recombinant GST-cCPE fusion protein (12).

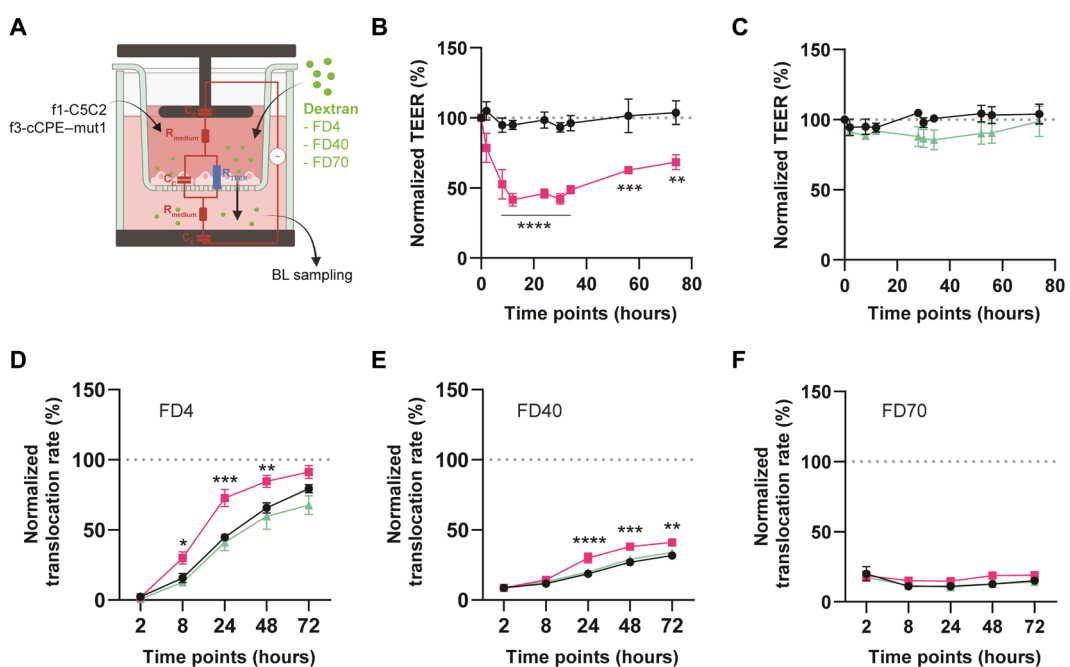
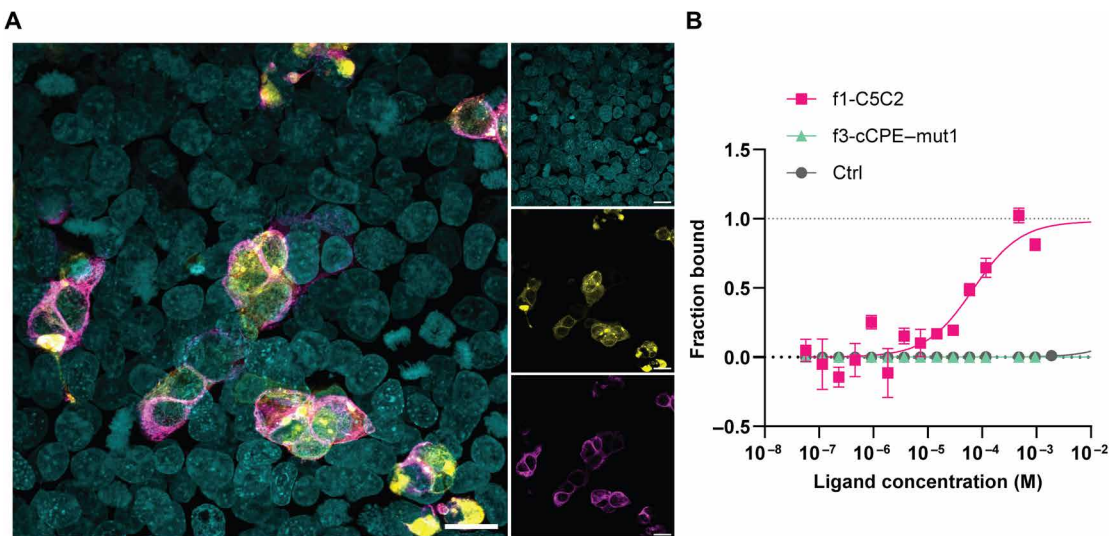


Fig. 6. Effect of the continuous exposure to selected peptides on the in vitro BBB properties. (A) Schematic representation of TEER experiments and 4/40/70 kDa fluorescein isothiocyanate–dextran transport studies. (B and C) TEER values (expressed as percentages of baseline values) for bEnd.3 cell layers continuously exposed to f1-C5C2 [(B) pink] and f3-cCPE-mut1 [(C) green] up to 72 hours. The vehicle was used as a control condition (black). (D to F) Normalized translocation rate for FD4 (D), FD40 (E), and FD70 (F) across bEnd.3 cell layers exposed to f1-C5C2 (pink), f3-cCPE-mut1 (green), or vehicle (black). Working concentrations for both peptides were 25 μ M. The translocation rate (expressed as a percentage of the translocation across a Transwell membrane in the absence of cells) was calculated from the ratio between the dextran mass in the basolateral side at the single time point and that in the apical side at $t = 0$. Data are means \pm SEM ($n = 3$). * $P < 0.05$, ** $P < 0.01$, *** $P < 0.001$, **** $P < 0.0001$.

As a complementary assay, we assessed the capability of fluorescein isothiocyanate-labeled dextran of different sizes (4 kDa for FD4, 40 kDa for FD40, and 70 kDa for FD70) to translocate across the barrier (Fig. 6, D to F). Notably, FD4 is a well-known hydrophilic marker for paracellular transport (62, 63). We incubated each molecule in the presence of either f1-C5C2 or f3-cCPE-mut1 (25 μ M) and monitored

their translocation rate (see more details in Materials and Methods) at various time points from 2 to 72 hours of incubation.

Data were expressed in percent of the maximum permeability that was determined in the absence of cells (empty Transwells), where the molecules were freely and equally distributed in the apical and basolateral compartments across the semipermeable membrane down

their concentration gradient. The progressive increase in the FD4 translocation through the cell barrier over time compared to control conditions indicates the presence of transcellular transport of the lowest molecular mass fluorescent tracer (Fig. 6D). The effect was decreased but still observable for FD40, while FD70 was not significantly transported in the presence of the BBB opening peptide (Fig. 6, E and F). f1-C5C2 showed a significant increase in the kinetics of transport of FD4 starting from 8 hours of incubation (Fig. 6, E and F), in good agreement with the observed decrease in TEER in the same time window. For FD40, the effect started to be significant after 24 hours of peptide exposure (Fig. 6E). This indicates that the opening of the paracellular spaces by the f1-C5C2 peptide exhibits size selectivity that represents a crucial aspect of avoiding an indiscriminate translocation of any species (including pathogens) to the brain during the paracellular opening window. When the f3-cCPE-mut1 peptide was used (green curve; Fig. 6, E and F), the transport behavior of all fluorescent dextrans did not differ from the control conditions.

To assess the efficacy of f1-C5C2 in a more physiologically relevant system, we set up a multicellular *in vitro* BBB model composed of a layer of pericytes and bEnd.3 cells on the opposite sides of a Transwell membrane (fig. S13A). As expected, in this model, TEER values significantly increased with respect to the bEnd.3 monoculture (fig. S13B), paralleled by CLDN5 overexpression by the endothelial cells (fig. S13C). Also in this configuration, the incubation with 25 μ M f1-C5C2 led to a significant decrease in TEER values after about 10 hours, although the effect was less pronounced than that observed on the bEnd.3 monoculture likely due to the increased tightness of the barrier (fig. S13D). No effect was observed on the pericytes monoculture that is not expressing CLDN5 (fig. S13E).

The decreased TEER values by the f1-C5C2 peptide are associated with internalization of CLDN5

mCLDN5 expression is linked to that of other TJ proteins, and all have a strict relation with the submembranous actin cytoskeleton (64–66). Thus, we quantified the total expression of mCLDN5, Occludin (OCLN), and Zonula occludens 1 (ZO1) through immunoblotting upon exposure to 10 and 25 μ M of f1-C5C2 for 24 hours, i.e., the temporal window in which TEER values showed the maximum decrease (Fig. 7, A to D). Both transmembrane proteins (mCLDN5 and OCLN) and the cytoplasmic scaffolding protein ZO-1 were significantly down-regulated after 24 hours of exposure to 25 μ M of the f1-C5C2 peptide, while actin remained unaltered. We then carried out immunofluorescence experiments to follow the subcellular trafficking of immunostained mCLDN5 over time upon exposure to the f1-C5C2 peptide (Fig. 7E). Quantitative confocal imaging analysis, reported in Fig. 7F (see fig. S14 for more details), showed that the cytoplasmic/membrane ratio of mCLDN5 in bEnd.3 cells increased significantly already after 6 to 8 hours of incubation with the f1-C5C2 peptide, indicating a marked internalization of the protein, consistent with the decrease in TEER values shown in Fig. 6A. This result was fully confirmed by surface biotinylation experiments in live bEnd.3 cells treated with either vehicle or the f1-C5C2 peptide for 24 hours, which showed that the biotinylated mCLDN5 fraction exposed on the plasma membrane was significantly decreased in favor of its cytosolic fraction that was correspondingly increased, in the absence of changes in the cytosolic and plasma membrane markers glyceraldehyde-3-phosphate dehydrogenase (GAPDH) and Na⁺/K⁺-ATPase-1, respectively (Fig. 7G).

Shorter exposure to the f1-C5C2 peptide is followed by a full recovery of the barrier integrity

The curve reported in Fig. 6B shows a tendency of the TEER values to return to control conditions after \approx 40 hours of c.i. with the f1-C5C2 peptide. However, the recovery of the barrier was not complete at longer time points (up to 72 hours), in line with other peptidomimetics attempts found in the literature (11, 37). Thus, we investigated whether a shorter “pulse” incubation (p.i., 8 hours) with the f1-C5C2 peptide, still effective in dropping TEER values, could allow a full recovery of TEER values and TJ integrity (Fig. 8A).

When the peptide was removed after reaching the barrier paracellular opening (8 hours), TEER values progressively rose and recovered the control values at 48 hours, while they were still significantly lower than the control for c.i. with the peptide (Fig. 8B). When we analyzed TJ proteins by immunoblotting at 48 hours, we found no significant changes in the total expression of mCLDN5, OCLN, and ZO1 for either continuous or pulsed exposure to the peptide (Fig. 8, C to E), indicating that the decrease in TJ protein expression observed at earlier times (24 hours, see Fig. 7, A to D) was recovered by bEnd.3 cells. However, quantification of cytoplasmic/membrane distribution of CLDN5 demonstrated that, while the c.i. with f1-C5C2 was still associated with a significantly larger internalization of CLDN5, the short pulsed exposure did not affect the membrane association of CLDN5 (Fig. 8C), consistent with the full recovery of barrier integrity.

DISCUSSION

The treatment of many neurological pathologies and the development of novel drugs against central nervous system-related disorders are still hampered by the limited delivery across the BBB. In this context, many strategies are under investigation to improve the passage of small molecules across the BBB, by enhancing either the transcellular or the paracellular pathways. The investigation of possible TJ-modulating strategies to enable small molecular weight drugs or nutrients to cross the BBB through the paracellular route is gaining increasing interest for its translational application in a variety of genetic or pathological brain conditions. Within BBB TJs, CLDN5 proteins are essential in sealing the paracellular space between two adjacent cells, and they could act as receptors to bind TJ modulators to enhance BBB permeability in a safe and reversible manner. TJ modulators hold clear advantages compared, for instance, to absorption enhancers (e.g., sodium caprate, chitosan, or alkylglycerols) (67, 68) as they can specifically and directly interact with the structural components of the TJs. Direct TJ modulators are mainly classified into two types: RNA interference agents and binding molecules (binders), which include derivatives of the nontoxic cCPE (12, 36, 37), peptidomimetics based on the mCLDN5 ECL1 domain (11, 37), and, in some cases, antibodies (69, 70). Peptide-based TJ modulators offer the opportunity of a widespread [opposite to localized approaches such as focused ultrasound-mediated BBB opening (71)] and transient action [given their short half-life in biological environments (72)], and also allow for flexible engineering. Compared to RNA interference, the peptidomimetic approach acts extracellularly, it does not directly interfere with the translation of CLDN5, and the dose-response might be more controllable.

In this work, we exploited this opportunity by setting up a synergistic *in silico*-*in vitro* platform, allowing for screening CLDN5-binding peptides presenting suitable solubility in biological media and efficient protein binding. We identified a short peptide of 14

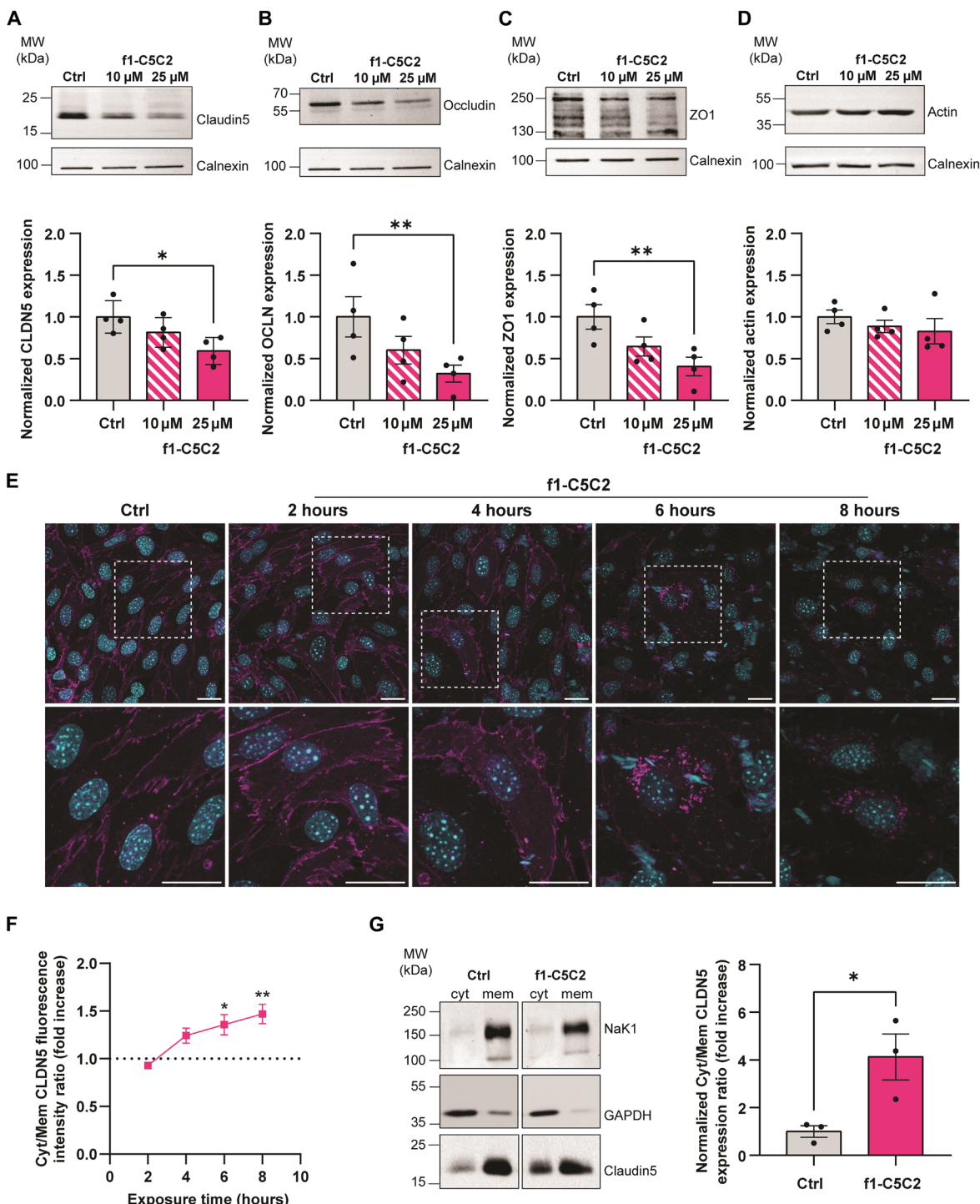


Fig. 7. Expression and translocation of TJ proteins upon exposure of bEnd.3 cells to the f1-C5C2 peptide. (A to D) Top, representative Western blots stained with CLDN5 [(A) 23 kDa], OCLN [(B) 55 kDa], ZO1 [(C) 220 kDa], actin [(D) 42 kDa], and calnexin (100 kDa) for bEnd.3 cells after 24 hours of exposure to either vehicle (Ctrl) or f1-C5C2 (10 and 25 μ M). Bottom, quantification of protein expression normalized over the respective controls. Data are means \pm SEM ($n = 4$), * $P < 0.05$, ** $P < 0.01$, one-way ANOVA/Dunnett's test. (E) Representative confocal images for CLDN5 immunostaining at various time points (2, 4, 6, and 8 hours) for bEnd.3 cells treated with vehicle (Ctrl) or exposed to 10 and 25 μ M f1-C5C2. The boxed areas are shown under each image at higher magnification. Scale bars, 25 μ m. (F) Quantitative image analysis CLDN5 subcellular distribution. The ratios between cytoplasmic and plasma membrane CLDN5 fluorescence intensity values at various time points (2, 4, 6, and 8 hours) were calculated per cell and normalized over the ratios of the respective controls. Data are means \pm SEM ($n = 3$ independent experiments in triplicates; five fields per replicate). * $P < 0.05$, ** $P < 0.01$, ordinary one-way ANOVA/Dunnett's test. (G) Surface biotinylation of bEnd.3 cells after 24 hours of exposure to either vehicle (Ctrl) or f1-C5C2 (25 μ M). Left, representative blots stained with antibodies to CLDN5 (18 kDa), the intracellular housekeeping protein GAPDH (36 kDa), and the plasma membrane-associated Na⁺/K⁺-ATPase 1 (NaK1, 130 kDa). Right, quantification of CLDN5 intracellular (cytosolic)/extracellular (membrane) expression normalized over the respective controls. Data are means \pm SEM ($n = 3$), * $P < 0.05$, unpaired Student's *t* test.

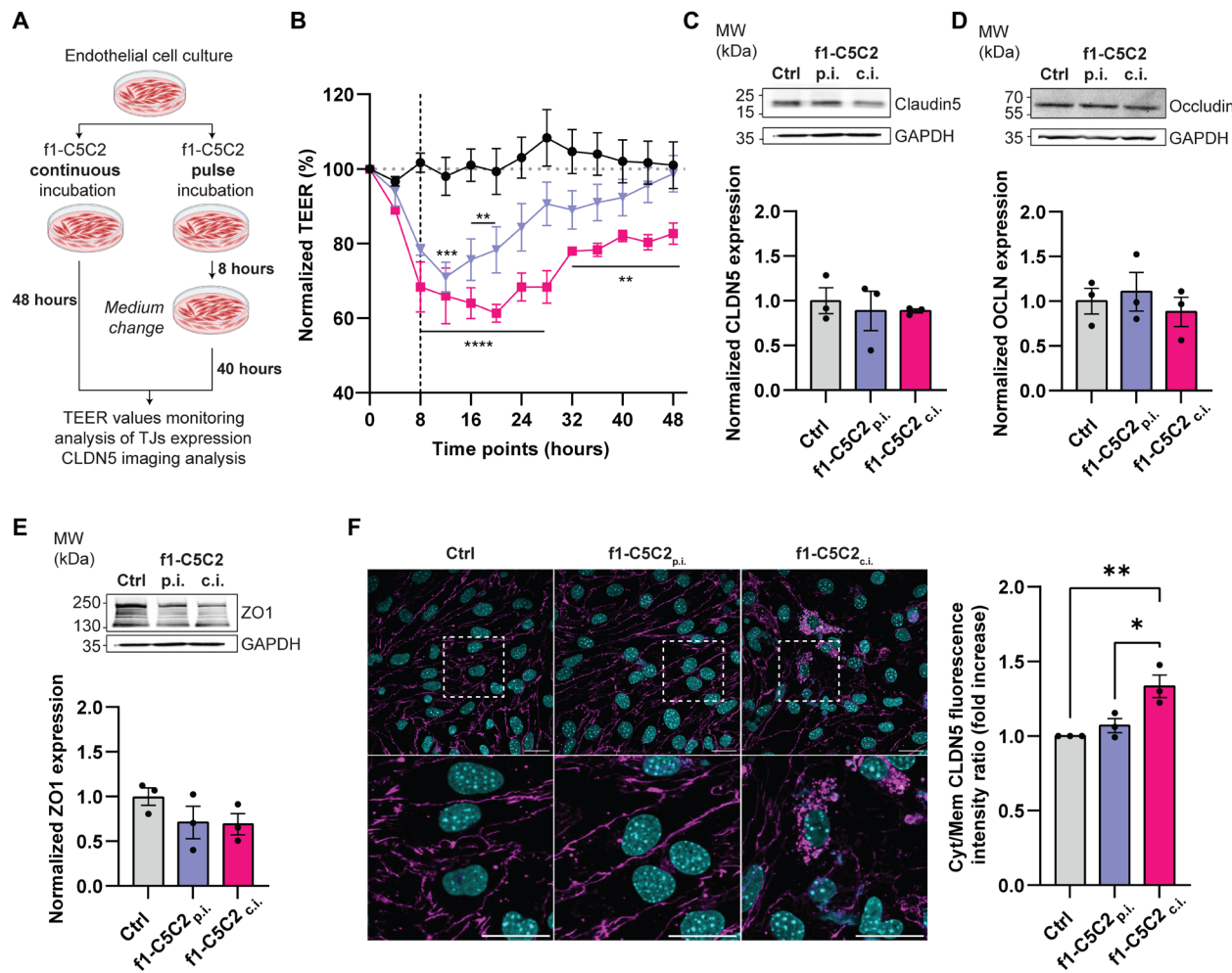


Fig. 8. Reversible opening of BBB upon pulsed exposure of bEnd.3 cells to the f1-C5C2 peptide. (A) Schematic of the experimental procedure for c.i. or p.i. exposure to the f1-C5C2 peptide. (B) TEER values (expressed in percent of baseline values) for bEnd.3 cell layers upon c.i. with f1-C5C2 (f1-C5C2_{c.i.}, pink) or 8 hour-pulsed incubation (f1-C5C2_{p.i.}, violet). Data are means \pm SEM ($n = 3$), ** $P < 0.01$, *** $P < 0.001$, **** $P < 0.0001$, two-way repeated measures ANOVA/Tukey's tests versus control conditions (vehicle). (C to E) Top, representative Western blots stained with CLDN5 [(C) 23 kDa], OCLN [(D) 55 kDa], ZO1 [(E) 220 kDa] observed at $t = 48$ hours for bEnd.3 cells treated with vehicle (Ctrl) or exposed to either p.i. or c.i. with the f1-C5C2 peptide (25 μ M), as described in (A). GAPDH (36 kDa) was used as a loading control. Bottom, quantification of protein expression normalized over the respective controls. Data are means \pm SEM ($n = 3$). (F) Left, representative confocal images of CLDN5 immunostaining at $t = 48$ hours for bEnd.3 cells treated with vehicle (Ctrl) or exposed to 25 μ M of either f1-C5C2_{c.i.} or f1-C5C2_{p.i.}. The boxed areas are reported under each image at higher magnification. Scale bars, 25 μ m. Right, quantitative analysis of CLDN5 subcellular distribution. The ratios between cytoplasmic and plasma membrane CLDN5 fluorescence intensity values were calculated per cell and normalized over the ratios of the respective controls. Data are means \pm SEM ($n = 3$ independent experiments in triplicates; five fields per replicate). * $P < 0.05$, ** $P < 0.01$, one-way ANOVA/Dunnett's tests versus control.

amino acids, here called f1-C5C2, and demonstrated that it is a valuable CLDN5-derived candidate for transient BBB permeabilization. The reduced size of the peptide constitutes a big advantage in terms of solubility and effective concentration to be used. Our data have shown that the peptide associates with the CLDN5 extracellular domain (11, 14, 73), recapitulating, for instance, the binding of cCPE derivatives to mCLDN5 (12) and to other crystallized CLDNs (39–41, 74).

Given the very short half-life of endogenous CLDN5 in endothelial cells (<90 min) (75), the role of the peptides would be to prevent the recruitment of additional CLDN5 monomers to the paracellular complex, thereby increasing paracellular delivery across the BBB. Previous reports are consistent with our observation that, following the tetramer complex opening, the mCLDN5-peptide

complexes can be endocytosed by brain endothelial cells (76–78). This mechanism would alter the distribution of mCLDN5 proteins at the membrane (cell-cell contact), thereby further impairing the integrity of TJ strands. This is a very important aspect that deserves further investigation in future works. While mislocalization of OCLN might initiate caspase activation (79), it has also been shown that down-regulation of total mCLDN5 expression by binding peptides might have beneficial effects in other pathological contexts, as previously reported for alcohol-fed rats (80). CLDN5 knockout strategies in mice, associated with increased paracellular transport of small molecules (800 to 1000 Da), showed no TJ breakdown or edema formation. Rather, after traumatic brain injury, CLDN5 knockout was associated with reduced focal cerebral edema and improved cognitive functions (81–83). Understanding the precise implication of TJ

dysregulation will be of pivotal importance to finely control this BBB opening tools.

In conclusion, we have shown the capability of a short C5C2-derived peptide to target and bind CLDN5 complexes with high specificity, inducing a lowering of TEER values and a transient and fully reversible increase in paracellular permeability to small molecules at low concentrations and short incubation times. We also set up a robust *in silico/experimental* workflow for the design and validation of competitive peptides to open CLDN5 multimeric assemblies that can be widely applied to any TJ protein. To convert these findings into feasible clinical applications, additional efforts are needed to fully understand and control the mechanism of action and the reversibility of the process. Despite a long way to go, we believe that our work sets a solid basis for the development of this promising field.

MATERIALS AND METHODS

Design of the peptide dataset

Starting from structural models of the mCLDN5-cCPE and multipore hCLDN5 complexes, we generated shorter fragments of either the bacterial toxin cCPE or the peptidomimetic C5C2 (11) by removing the segments not directly interacting with CLDN5. We obtained three peptides from cCPE (f1-cCPE, f2-cCPE, and f3-cCPE) and two from C5C2 (f1-C5C2 and f2-C5C2). Then, we introduced single-point mutations in the resulting sequences to enhance their hydrophilicity, generating the peptides data bank shown in table S1. A detailed description of the procedure adopted to design each oligomer is provided in section S3, whereas the generation of hCLDN5 triple-pore models, based on the strategy used in our previous works (25, 27, 28, 31, 32), is illustrated in section S4.

Peptide structure prediction, equilibration, and computational assessment of water solubility

After *de novo* modeling and preliminary relaxation, each peptide was solvated and equilibrated for 100 ns by standard MD simulations in the NPT ensemble at $T = 303.15\text{ K}$ and $P = 1\text{ bar}$ maintained by a Langevin thermostat and Nosé-Hoover Langevin barostat (84, 85). Simulations were performed with the CHARMM36m force field (86) and the NAMD 3.0 program (87). More details on the procedure are reported in section S5.

To predict the propensity of the peptides listed in table S1 to either form aggregates or remain adequately dispersed when immersed in water, we devised a computational strategy based on the introduction of descriptors for molecular aggregates formed in the simulations, as described in prior work (88). The full protocol is sketched in fig. S2 and discussed in section S6.

MD simulations of the mCLDN5-peptide complexes

Because of the absence of an experimental template, the mCLDN5 monomeric structure was generated by homology modeling using either the mCLDN15 [PDB ID: 4P79 (38)] or the hCLDN4 (PDB ID: 5B2G) crystal structures as templates. After the refinement of the model via all-atom MD simulations (see section S7), the equilibrated configuration of the protein was used as a receptor to produce an initial pose for the mCLDN5-peptide complexes with f1-C5C2 and f3-cCPE-mut1 using molecular docking calculations. Since the number of dihedral angles in our ligands is larger than that allowed in the docking program, we used an iterative procedure

based on the optimization of poses for adjacent peptide segments. Details are reported in section S8. Selected models for the mCLDN5-f1-C5C2 and the mCLDN5-f3-cCPE-mut1 systems were then embedded in a 1-palmitoyl-2-oleyl-sn-glycero-3-phosphocholine lipid bilayer, solvated with water and a 0.15 M KCl ionic bath. After a preliminary equilibration of 30 ns, 200 ns of MD simulations were performed with NAMD 3.0 (87) and the CHARMM36m force field (89) in the NPT ensemble at $T = 310\text{ K}$ and $P = 1\text{ bar}$ maintained by a Langevin thermostat and the Nosé-Hoover Langevin piston pressure control (84, 85). During production, the protein was restrained from lateral movement, and the peptide rearrangement was confined in a cylindrical region to prevent lateral diffusion, as shown in fig. S5. The two MD trajectories were analyzed with VMD 1.9.3 (90) for structural descriptors and can be visualized in the movie S1. Additional details of the standard MD simulations and the analysis are provided in section S9.

CLDN-peptides unbinding MD simulations

Enhanced sampling approaches can largely increase the efficiency of MD simulations, in particular for highly flexible systems such as protein-peptide complexes (53, 54, 91–94). Several techniques can be used to speed up the conformational sampling of the peptide and accelerate its escape from the energy minimum in the binding site, rarely seen in standard MD simulations (93). Some of the options include applying a higher temperature to selected degrees of freedom (55, 95), using constant (96) or adaptive (95) biasing potentials, or canceling the mean force acting on the CVs (97, 98). Here, FE profiles for peptide unbinding from mCLDN5 were calculated using TAMD simulations (55, 56), taking as CV the distance between the COMs of the peptides and the mCLDN5's ECL, mapped in a range from 8 to 30 Å. The lateral diffusion of the peptide was limited by a cylindrical restraint, as done already in standard MD simulations (fig. S2). The use of spatial restraints was recommended in previous works (91, 99–103) to ensure a faster convergence of the calculations, and their effect must be taken into account when computing the K_d (see below). While TAMD is an efficient method to enhance sampling (95, 104), other techniques have been developed to obtain the FE from a TAMD trajectory by integrating the mean forces acting on each CV (i.e., minus the derivative of the FE), such as the single-sweep (105, 106) and the on-the-fly parametrization methods (107, 108). Here, TAMD was performed using the Colvars module (109) via the extended Lagrangian dynamics feature for the CV (110), and the FE was computed from the mean forces collected along the runs (57). More details on the approach and its implementation are reported in section S10. To validate the FE profiles obtained from TAMD, we calculated them also using the extended-system eABF approach (57, 97). Last, the mCLDN5-f1-C5C2 FE curve from TAMD was used to predict the K_d . Further information on eABF and the calculation of K_d are provided in section S10.

Clustering structures

Representative structures of the mCLDN5-peptide complex obtained from TAMD simulations were selected by filtering the configurations showing a distance between the peptide and the mCLDN5 extracellular COMs corresponding to the FE minimum $\pm 0.5\text{ \AA}$. The resulting structures were grouped in clusters based on the RMSD of the peptides, calculated with respect to the final configuration resulting from the standard MD simulation. In each cluster, a threshold of 2.5 \AA was chosen, thus generating six ensembles ranging from 0 to 15 Å. The center of

each cluster was selected as a representative structure of the sampling performed during the TAMD simulations. The same clustering procedure was performed for the eABF structures, although they were not used for further investigations.

Peptide synthesis and MS analysis of peptide solubility

All peptides were custom-synthesized by Proteogenix. A 7.5 mM stock solution in H₂O/ACN 1:1 was prepared and kept at -20°C. For experiments with cells, dilutions from the stock were prepared in fresh cell culture medium and sonicated for 5 min in an ultrasonic bath. H₂O/ACN 1:1 at the same dilution was used as a control.

f1-C5C2, f2-C5C2, f3-cCPE-mut1 peptides were dissolved in Milli-Q water for the preparation of 1 mM stock solution for each peptide. For an external calibration, eight standard solutions for each peptide were prepared in H₂O/ACN 1:1 (10 pM, 100 pM, 1 nM, 10 nM, 100 nM, 1 μM, 10 μM, and 30 μM). For these calibrators, a 100% solubility was assumed and used as a reference. Each peptide sample was then diluted in either Milli-Q water or DMEM to reach a concentration of 25 μM and left for 1 hour at 37°C before LC-MS analysis. All data were acquired on a Waters ACQUITY Single Quadrupole Detector, coupled with a Waters Acquity UPLC system. Peptides were loaded on Acquity UPLC BEH C18 column (2.1 mm by 50 mm, 1.7-μm particle size). Ionization was conducted by positive electrospray ionization mode; the capillary voltage was set to 2.5 kV and the cone voltage to 35 V. Selected ion recording of two masses ([M + 3H]³⁺ = 606.1; [M + 2H]²⁺ = 908.5) for f3-cCPE-mut1, one ([M + 2H]²⁺ = 756.3) for f1-C5C2 and one ([M + 2H]²⁺ = 648.3) for f2-C5C2, was used as mass detection for the specific peptide. The calculation of the final concentration in each sample was performed by extrapolating it from the calibration curve using TargetLynx software (Waters).

Cell culture and transfection procedures

Immortalized mouse brain endothelial cells (bEnd.3) were purchased from American Type Culture Collection (ATCC CRL2299). The cells were cultured in DMEM supplemented with 10% fetal bovine serum (FBS), 1% penicillin-streptomycin, and 1% glutamine. The cells were grown in T75 culture flasks and maintained in 5% CO₂, 90% humidified atmosphere at 37°C. The cell culture medium was replaced every 2 days, and the cells were maintained between passages 25 and 30. For the monolayer, the cells were seeded onto collagen-coated upper Transwell membranes (150 μg/ml; 12-mm Ø inserts, pore size 0.4 μm, growth area 1.12 cm²; Transwell 3460 Corning Costar) or onto 18-mm Ø glass coverslips at the density of 40 × 10³ cells per well. The cell culture medium was replaced twice a week. All reagents were purchased from Thermo Fisher Scientific, unless specified. HEK cells line 293 expressing the large T antigen of simian virus 40 (SV40) (HEK 293T) were purchased from ICLC (HTL04001). The cells were cultured in DMEM supplemented with 10% FBS, 1% penicillin-streptomycin, and 1% glutamine. For transfection, the cells were plated on poly-D-lysine (10 μg/ml)-coated petri dishes 24 hours before the experiment. HEK293T cells were seeded in T75 flask and transfected at 80%. To prepare lipoplexes, 100 μl of Lipofectamine 2000 in DMEM was added with 40 μg of pDNA (mCLDN5 tGFP-tagged, Origene #MG202442) and incubated for 20 min at room temperature (RT). The transfection complexes were added to cells and incubated for 6 hours at 37°C. The medium was then replaced by fresh medium, and the cells were incubated for an additional 24 hours before lysis and binding studies.

The total protein amount of cell lysate was evaluated by measuring absorbance at 280 nm using a NanoDrop 2000 (Thermo Fisher Scientific). The total GFP amount was estimated through a calibration curve obtained by measuring the fluorescence intensity of the recombinant tGFP protein (*Pontellina plumata*, catalog no.: TP700079, Origene) at increasing concentrations with a Tecan SPARK (Tecan, Switzerland) multimode microplate reader.

Cell lysate preparation

Among various lysis methods explored to maintain the highest GFP fluorescent signal, flash freeze-thawing in liquid nitrogen was selected as it performed similarly to radioimmunoprecipitation assay (RIPA) lysis (see GFP emission spectra in fig. S12) but allowing us to keep cells in phosphate-buffered saline (PBS), thus avoiding buffer exchange before MST analysis. The total protein concentration in the lysates was determined spectrophotometrically, and the GFP content was estimated through a fluorescence calibration curve of the recombinant tGFP (fig. S13). To exclude the presence of nonspecific binding due to GFP, nontransfected HEK-293T cell lysates with a comparable concentration of spiked recombinant tGFP were used as control.

Microscale thermophoresis

HEK293T cells transfected with mCLDN5-GFP were washed in PBS, detached with trypsin, and centrifuged (5 min, 200g). Pellets were resuspended in PBS and lysed through flash freeze-thawing in liquid nitrogen. Cell suspensions were then repeatedly passed through a 25-G needle (five times), followed by five times through a 27-G needle, and finally centrifuged (10 min, 2800g, 4°C). To evaluate mCLDN5 binding, the peptides (ligand), diluted in PBS/Tween-20 (0.1%), were added in defined amounts as titration series (15 serial 1:2 dilutions starting from 400 μM) to cell lysates containing mCLDN5-GFP (target, 1 μM). The samples were then loaded into Premium capillaries (Monolith Series, #MO-K025, NanoTemper), and the fluorescence signal was measured with a Monolith NT.115, NanoTemper (Nano-BLUE laser, power 20 to 30%). Binding was characterized by the K_d and the analysis was performed using the MO.Affinity Analysis software (NanoTemper), using the K_d fit model that describes a molecular interaction with a 1:1 stoichiometry according to the law of mass action. In the case of a binding event, the fraction bound is defined by the binding affinity K_d and the concentration of the target molecule and depends on the ligand concentration

$$f_c = \frac{c + c_T + K_d - \sqrt{(c + c_T + K_d)^2 + 4 c c_T}}{2 c_T}$$

being f_c the fraction bound at a given ligand concentration c , and c_T the final concentration of the target (constant). Assuming that $c_T < < K_d$, the K_d is typically identical to the inflection point (half maximal effective concentration) of the F_{norm} , which is calculated by dividing fluorescence values from the temperature-related intensity change trace after the laser is turned on (hot region) by values that are obtained before the laser is turned on (the initial fluorescence or cold region). However, in our case, the ligand induces a change in initial fluorescence, and this influence on the F_{norm} is accounted for in the DI.Screening Analysis software. The K_d was also recalculated

by fitting the curves by nonlinear regression (one site-specific binding) on GraphPad PRISM 10, finding comparable results.

Cell viability

bEnd.3 cells were treated with selected peptides (25 μ M) for 24 hours. After washing, the cells were incubated for 5 min with Hoechst33342 (1 μ M) for nuclear visualization, calcein-AM (1 μ M) for cell viability, and propidium iodide (1 μ M) for cell death quantification. Cell viability was quantified by using a Nikon Eclipse-80i upright epifluorescence microscope at 10 \times magnification. About 10 fields were randomly selected for each independent culture ($n = 2$). Image analysis was performed using the Cell Profiler software (Broad Institute).

Cocultures on Transwell membrane

On day one, the apical side of Transwell inserts (12 mm Ø inserts, pore size 0.4 μ m, growth area 1.12 cm 2 ; Transwell 3460 Corning Costar) was coated with collagen (150 μ g/ml), while the basolateral side with poly-L-lysine (10 μ g/ml; 1 hour, 37°C, 5% CO₂ for both coating conditions). Mouse brain vascular pericytes from CD57BL/6 were prestained with CellTracker Green CMFDA Dye (Invitrogen, #C2925) and subsequently seeded onto the previously coated basolateral side of flipped Transwell membranes with a drop at a density of 60×10^4 cells per well. The plates were returned to the incubator for 2 hours to let the cells adhere. Then, the inserts were reverted, any excess medium was removed, and both apical and basolateral compartments were filled with pericyte medium. Two days later, the pericytes medium on the apical side was removed and the bEnd.3 cells were seeded on the apical side at the density of 80×10^4 cells per well in supplemented DMEM, while the pericyte medium in the basolateral compartment was renewed. TEER measurements were used to evaluate correct barrier formation. When the barrier reached stable plateau TEER values, CLDN5 immunostaining, Western blot, and incubation with f1-C5C2 peptide were performed. Larger inserts (24 mm Ø, pore size 0.4 μ m, growth area 4.67 cm 2 ; Transwell 3450 Corning Costar) were used for Western blotting analysis, following the procedure described above, to ensure that a suitable number of cells and bEnd.3 cell monolayer was used as a control for CLDN5 expression. For exposure to f1-C5C2, the pericyte monoculture was used as a control.

Immunofluorescence

bEnd.3 or HEK293T monolayers, grown and treated either on glass coverslips or on plastic black 96-well culture plates (μ -Plate 96 Well Square, Ibidi, 89626), were fixed in 4% paraformaldehyde in PBS for 15 min at RT. The cells were permeabilized with 0.1% Triton X-100 for 5 min, blocked with 2% bovine serum albumin (BSA) for 30 min at RT, and incubated with the primary antibody (rabbit polyclonal anti-CLDN5, Invitrogen, #PA599415, 1:500) in the same blocking solution for 3 hours. After several PBS washes, the cells were incubated for 1 hour with the appropriate secondary antibodies (Molecular Probes, Thermo Fisher Scientific) diluted 1:500 in the blocking buffer solution. Last, the cells were incubated for 5 min with Hoechst (1 μ M, #3342, Sigma-Aldrich) for nuclear visualization and mounted with Vectashield antifade mounting medium (#H-1000-10, Vector Laboratories) on microscope slides. After CLDN5 immunostaining, the images were acquired using a laser-scanning confocal microscope (SP8, Leica microsystem GmbH, Wetzlar, German) at 63 \times magnification. For each set of experiments, all images were acquired using identical exposure settings. Five fields and an equal number of z-stacks for each sample were considered. Maximal projection images were then

analyzed on CellProfiler, using a custom-made pipeline able to distinguish intracellular and extracellular CLDN5 based on intensity and morphology.

TEER measurements and transport studies

The cells were grown until reaching a plateau in the TEER values of about 10 to 15 ohm·cm 2 . At this point, the apical fraction was replaced with a solution of 25 μ M peptides or vehicle. The peptide was left for all the time of the experiment in the case of c.i., or removed after 8 hours by replacing the culture medium in the case of p.i. TEER values were monitored every hour for 72 hours using a Cell-Zscope+ instrument (NanoAnalytics, Münster, Germany).

Transport studies were performed by measuring the 4/40/70 kDa fluorescein isothiocyanate-dextran (FD4, #46944, FD40, FD70, Merk) translocated mass at 2, 8, 24, 48, and 72 hours. Before each experiment, the Transwell apical medium was replaced with FD4/40/70 (40 μ g/ml) in the presence of either 25 μ M f1-C5C2 or f3-cCPE-mut1. The basolateral compartment was filled with 1.5 ml of fresh medium. At the indicated time points, 100 μ l of aliquots were sampled from the basolateral chamber into a 96-wells plate and immediately replaced by 100 μ l of fresh cell medium to maintain the total volume. Fluorescence measurements were conducted using a Tecan SPARK (Tecan, Switzerland) multimode microplate reader using the 485-nm fluorescein isothiocyanate channel for excitation and reading the fluorescence emission at 535 nm. Serial dilutions of FD4/40/70 in the range of 0 to 300 μ g/ml in cell medium were prepared to obtain a calibration curve. Linear regression was applied to define the correlation between fluorescence intensity and FD4/40/70 mass concentration and used to determine the total mass of FD4/40/70 in the basolateral chamber. The regression coefficients obtained from the linear curve fits were generally 0.98 to 0.99 ($n = 3$ wells, from three independent culture preparations). The translocation rate was calculated from the ratio between the translocated dextran mass at the single time point and the mass of dextran in the apical side at $t = 0$ and normalized as the percentage of the transport across a Transwell membrane in the absence of cells.

Western blotting of TJ proteins

bEND.3 cells were grown on six-well plates until reaching confluence and then treated with various concentrations and for various incubation times with the f1-C5C2 peptide. One or 2 days after the beginning of the peptide incubation, the cells were washed three times in cold PBS. bEnd.3 cells were lysed by adding RIPA buffer [50 mM tris-HCl (pH 7.4), 150 mM NaCl, 1% Igepal, 0.1% SDS, and 0.5% sodium deoxycholate] supplemented with protease inhibitors (complete EDTA-free protease inhibitors, Roche Diagnostic, Monza, Italy) and phosphatases inhibitors (serine/threonine phosphatase inhibitor and tyrosine phosphatase inhibitor, Sigma-Aldrich) and by scraping them off. Cell lysates were sonicated for 10 s (Branson SLPe; 25% amplitude) and centrifuged (4°C, 19,000g, 15 min). Supernatants were collected, and the total amount of proteins was calculated by the BCA Protein Assay kit (Thermo Fisher Scientific) using a BSA standard curve. The samples were denatured for 5 min at 95°C and separated by SDS-polyacrylamide gel electrophoresis (SDS-PAGE; 5% and 8 to 12% acrylamide in the stacking and running gels, respectively). After the run, the samples were transferred onto a nitrocellulose membrane (Amersham Protran, Cytiva) for 90 min at 100 V at 4°C. The membranes were blocked with 5% milk solution in tris-buffered saline containing 0.05% Tween-20 (0.05% TBS-T) for 1 hour at RT and then incubated overnight

with antibodies against: ZO-1 (rabbit polyclonal antibody, Invitrogen, #61-7300), OCLN (mouse monoclonal antibody, Invitrogen, #33-1500, 1:1000), CLDN5 (rabbit polyclonal, Invitrogen, #PA599415, 1:500), and the housekeeping protein calnexin (rabbit polyclonal antibody, Enzo Life Sciences, ADI-SPA-860, 1:1000). After three washes with 0.05% TBS-T, the membranes were incubated with horseradish peroxidase-conjugated secondary antibodies (Abcam, 1:10000) for 1 hour at RT and developed using the ECL Prime Western Blotting System (Amersham Protran, Cytiva). The chemiluminescent signals were revealed using the iBright FL1500 Imaging System (Thermo Fisher Scientific, A44241), and band intensities were analyzed with iBright Analysis Software.

Surface biotinylation

bEND.3 cells cultured on three-well plates until confluence were either treated with either vehicle or the f1-C5C2 peptide (25 μ M) for 24 hours. Then, the cells were washed in cold PBS and incubated for 30 min with EZ-Link Sulfo-NHS-LC-biotin (1 mg/ml; Thermo Fisher Scientific, 21335) in cold PBS (pH 8). Biotinylated cells were washed twice in 50 mM tris-HCl (pH 8) and twice in cold PBS (pH 8) to eliminate unbound biotin and then lysed in RIPA buffer. A portion of the lysate supernatants was kept for the total (input) sample, while the remaining volume was added with 100 μ l of NeutrAvidin-conjugated agarose beads (Thermo Fisher Scientific, 29201) and incubated for 3 hours at 4°C with constant rotation. After centrifugation, intracellular proteins were collected from the supernatants, while pellets were washed twice in RIPA buffer and twice in PBS before eluting the extracellularly labeled membrane proteins. Input, cytosolic and extracellular fractions were separated by SDS-PAGE, transferred to nitrocellulose membranes (Amersham Protran, Cytiva) as described above. The membranes were then incubated overnight with antibodies against CLDN5 (rabbit polyclonal, Invitrogen, #PA599415, 1:500) and the housekeeping cytosolic protein GAPDH (rabbit polyclonal, Abcam 9485, 1:5000) and the plasma membrane protein NaK1 (mouse monoclonal, Millipore, 05-369, 1:2000). Membranes were developed using the ECL Prime Western Blotting System (Amersham Protran, Cytiva) and analyzed as described above.

Statistical analysis

Statistical analysis was carried out using Prism v9 (GraphPad Software). Data are expressed as means \pm SEM for a number of independent experiments (n) with superimposition of the individual experimental points. Normal distribution was assessed using the D'Agostino-Pearson normality test. To compare two normally distributed sample groups, the one- or two-tailed Student's t test was used. To compare more than two normally distributed sample groups, two-way repeated measures analysis of variance (ANOVA) followed by Tukey's multiple comparisons test was used. To compare more than two nonnormally distributed sample groups, one-way Friedman's ANOVA followed by Dunn's multiple comparison test was used.

Supplementary Materials

This PDF file includes:

Sections S1 to S10

Figs. S1 to S14

Legend for movie S1

Tables S1 to S4

References

Other Supplementary Material for this manuscript includes the following:

Movie S1

REFERENCES AND NOTES

- C. Greene, M. Campbell, Tight junction modulation of the blood brain barrier: CNS delivery of small molecules. *Tissue Barriers* **4**, e1138017 (2016).
- W. M. Pardridge, The blood-brain barrier: Bottleneck in brain drug development. *NeuroRx* **2**, 3–14 (2005).
- H. Koch, Y. G. Weber, The glucose transporter type 1 (Glut1) syndromes. *Epilepsy Behav.* **91**, 90–93 (2019).
- M. Tang, S. H. Park, D. C. De Vivo, U. R. Monani, Therapeutic strategies for glucose transporter 1 deficiency syndrome. *Ann. Clin. Transl. Neurol.* **6**, 1923–1932 (2019).
- D. Wang, J. M. Pascual, D. D. Vivo, *Glucose Transporter Type 1 Deficiency Syndrome* (University of Washington, 2018; <https://ncbi.nlm.nih.gov/sites/books/NBK1430/>).
- Y. Hashimoto, M. Campbell, Tight junction modulation at the blood-brain barrier: Current and future perspectives. *Biochim. Biophys. Acta Biomembr.* **1862**, 183298 (2020).
- K. Ogawa, N. Kato, S. Kawakami, Recent strategies for targeted brain drug delivery. *Chem. Pharm. Bull.* **68**, 567–582 (2020).
- S. Bergmann, S. E. Lawler, Y. Qu, C. M. Fadzen, J. M. Wolfe, M. S. Regan, B. L. Pentelute, N. Y. R. Agar, C.-F. Cho, Blood-brain-barrier organoids for investigating the permeability of CNS therapeutics. *Nat. Protoc.* **13**, 2827–2843 (2018).
- M.-A. Bellavance, M. Blanchette, D. Fortin, Recent advances in blood-brain barrier disruption as a CNS delivery strategy. *AAPS J.* **10**, 166–177 (2008).
- A. Goliaei, U. Adhikari, M. L. Berkowitz, Opening of the blood-brain barrier tight junction due to shock wave induced bubble collapse: A molecular dynamics simulation study. *ACS Chem. Neurosci.* **6**, 1296–1301 (2015).
- S. Dithmer, C. Staat, C. Müller, M.-C. Ku, A. Pohlmann, T. Niendorf, N. Gehne, P. Fallier-Becker, Á. Kittel, F. R. Walter, S. Veszelka, M. A. Deli, R. Blasig, R. F. Haseloff, I. E. Blasig, L. Winkler, Claudin peptidomimetics modulate tissue barriers for enhanced drug delivery. *Ann. N. Y. Acad. Sci.* **1397**, 169–184 (2017).
- W. Neuhaus, A. Piontek, J. Protze, M. Eichner, A. Mahringer, E.-A. Subileau, I.-F. M. Lee, J. D. Schulzke, G. Krause, J. Piontek, Reversible opening of the blood-brain barrier by claudin-5-binding variants of Clostridium perfringens enterotoxin's claudin-binding domain. *Biomaterials* **161**, 129–143 (2018).
- Z. Liao, Z. Yang, A. Piontek, M. Eichner, G. Krause, L. Li, J. Piontek, J. Zhang, Specific binding of a mutated fragment of Clostridium perfringens enterotoxin to endothelial claudin-5 and its modulation of cerebral vascular permeability. *Neuroscience* **327**, 53–63 (2016).
- C. Staat, C. Coisne, S. Dabrowski, S. M. Stamatovic, A. V. Andjelkovic, H. Wolburg, B. Engelhardt, I. E. Blasig, Mode of action of claudin peptidomimetics in the transient opening of cellular tight junction barriers. *Biomaterials* **54**, 9–20 (2015).
- D. Zwanziger, D. Hackel, C. Staat, A. Böcker, A. Brack, M. Beyermann, H. Rittner, I. E. Blasig, A peptidomimetic tight junction modulator to improve regional analgesia. *Mol. Pharm.* **9**, 1785–1794 (2012).
- S. N. Aasen, H. Espedal, C. F. Holte, O. Keunen, T. V. Karlset, O. Tenstad, Z. Maherally, H. Miletic, T. Hoang, A. V. Eikeland, H. Baghirov, D. E. Olberg, G. J. Pilkington, G. Sarkar, R. B. Jenkins, T. Sundström, R. Bjerkvig, F. Thorsen, Improved drug delivery to brain metastases by peptide-mediated permeabilization of the blood-brain barrier. *Mol. Cancer Ther.* **18**, 2171–2181 (2019).
- R. M. Jones, K. Hynynen, Advances in acoustic monitoring and control of focused ultrasound-mediated increases in blood-brain barrier permeability. *Br. J. Radiol.* **92**, 20180601 (2019).
- Q. Cai, X. Li, H. Xiong, H. Fan, X. Gao, V. Vemireddy, R. Margolis, J. Li, X. Ge, M. Giannotta, K. Hoyt, E. Maher, R. Bachoo, Z. Qin, Optical blood-brain-tumor barrier modulation expands therapeutic options for glioblastoma treatment. *Nat. Commun.* **14**, 4934 (2023).
- A. Berselli, F. Benfenati, L. Maragliano, G. Alberini, Multiscale modelling of claudin-based assemblies: A magnifying glass for novel structures of biological interfaces. *Comput. Struct. Biotechnol. J.* **20**, 5984–6010 (2022).
- J. Piontek, S. M. Krug, J. Protze, G. Krause, M. Fromm, Molecular architecture and assembly of the tight junction backbone. *Biochim. Biophys. Acta Biomembr.* **1862**, 183279 (2020).
- G. Krause, L. Winkler, S. L. Mueller, R. F. Haseloff, J. Piontek, I. E. Blasig, Structure and function of claudins. *Biochim. Biophys. Acta Biomembr.* **1778**, 631–645 (2008).
- S. Amasheh, T. Schmidt, M. Mahn, P. Florian, J. Mankertz, S. Tavalali, A. H. Gitter, J.-D. Schulzke, M. Fromm, Contribution of claudin-5 to barrier properties in tight junctions of epithelial cells. *Cell Tissue Res.* **321**, 89–96 (2005).
- F. J. Irudayanathan, N. Wang, X. Wang, S. Nangia, Architecture of the paracellular channels formed by claudins of the blood-brain barrier tight junctions. *Ann. N. Y. Acad. Sci.* **1405**, 131–146 (2017).
- F. J. Irudayanathan, S. Nangia, Paracellular gatekeeping: What does it take for an ion to pass through a tight junction pore? *Langmuir* **36**, 6757–6764 (2020).
- A. Berselli, G. Alberini, F. Benfenati, L. Maragliano, Computational assessment of different structural models for Claudin-5 complexes in blood-brain barrier tight junctions. *ACS Chem. Neurosci.* **13**, 2140–2153 (2022).

26. H. Suzuki, K. Tani, A. Tamura, S. Tsukita, Y. Fujiyoshi, Model for the architecture of Claudin-based paracellular ion channels through tight junctions. *J. Mol. Biol.* **427**, 291–297 (2015).
27. G. Alberini, F. Benfenati, L. Maragliano, A refined model of claudin-15 tight junction paracellular architecture by molecular dynamics simulations. *PLOS ONE* **12**, e0184190 (2017).
28. G. Alberini, F. Benfenati, L. Maragliano, Molecular dynamics simulations of ion selectivity in a Claudin-15 paracellular channel. *J. Phys. Chem. B* **122**, 10783–10792 (2018).
29. S. K. Nagarajan, J. Piontek, Molecular dynamics simulations of Claudin-10a and -10b ion channels: With similar architecture, different pore linings determine the opposite charge selectivity. *Int. J. Mol. Sci.* **25**, 3161 (2024).
30. S. K. Nagarajan, S. Klein, B. S. Fadakar, J. Piontek, Claudin-10b cation channels in tight junction strands: Octameric-interlocked pore barrels constitute paracellular channels with low water permeability. *Comput. Struct. Biotechnol. J.* **21**, 1711–1727 (2023).
31. A. Berselli, G. Alberini, F. Benfenati, L. Maragliano, Computational study of ion permeation through claudin-4 paracellular channels. *Ann. N. Y. Acad. Sci.* **1516**, 162–174 (2022).
32. A. Berselli, G. Alberini, F. Benfenati, L. Maragliano, The impact of pathogenic and artificial mutations on Claudin-5 selectivity from molecular dynamics simulations. *Comput. Struct. Biotechnol. J.* **21**, 2640–2653 (2023).
33. R. J. Mrsny, G. T. Brown, K. Gerner-Smidt, A. G. Buret, J. B. Meddings, C. Quan, M. Koval, A. Nasrat, A key claudin extracellular loop domain is critical for epithelial barrier integrity. *Am. J. Pathol.* **172**, 905–915 (2008).
34. M. Kondoh, A. Takahashi, M. Fujii, K. Yagi, Y. Watanabe, A novel strategy for a drug delivery system using a claudin modulator. *Biol. Pharm. Bull.* **29**, 1783–1789 (2006).
35. A. Takahashi, M. Kondoh, A. Masuyama, M. Fujii, H. Mizuguchi, Y. Horiguchi, Y. Watanabe, Role of C-terminal regions of the C-terminal fragment of Clostridium perfringens enterotoxin in its interaction with claudin-4. *J. Control. Release* **108**, 56–62 (2005).
36. J. Protze, M. Eichner, A. Piontek, S. Dinter, J. Rossa, K. G. Blecharz, P. Vajkoczy, J. Piontek, G. Krause, Directed structural modification of Clostridium perfringens enterotoxin to enhance binding to claudin-5. *Cell. Mol. Life Sci.* **72**, 1417–1432 (2015).
37. L. Chen, R. Sutharsan, J. L. Lee, E. Cruz, B. Asnicar, T. Palliyaguru, J. M. Wasieleska, A. Gaudin, J. Song, G. Leinenga, J. Götz, Claudin-5 binder enhances focused ultrasound-mediated opening in an in vitro blood-brain barrier model. *Theranostics* **12**, 1952–1970 (2022).
38. H. Suzuki, T. Nishizawa, K. Tani, Y. Yamazaki, A. Tamura, R. Ishitani, N. Dohmae, S. Tsukita, O. Nureki, Y. Fujiyoshi, Crystal structure of a claudin provides insight into the architecture of tight junctions. *Science* **344**, 304–307 (2014).
39. T. Shinoda, N. Shinya, K. Ito, N. Ohsawa, T. Terada, K. Hirata, Y. Kawano, M. Yamamoto, T. Kimura-Someya, S. Yokoyama, M. Shirouzu, Structural basis for disruption of claudin assembly in tight junctions by an enterotoxin. *Sci. Rep.* **6**, 33632 (2016).
40. S. Nakamura, K. Irie, H. Tanaka, K. Nishikawa, H. Suzuki, Y. Saitoh, A. Tamura, S. Tsukita, Y. Fujiyoshi, Morphologic determinant of tight junctions revealed by claudin-3 structures. *Nat. Commun.* **10**, 816 (2019).
41. A. J. Vecchio, R. M. Stroud, Claudin-9 structures reveal mechanism for toxin-induced gut barrier breakdown. *Proc. Natl. Acad. Sci. U.S.A.* **116**, 17817–17824 (2019).
42. G. Weng, J. Gao, Z. Wang, E. Wang, X. Hu, X. Yao, D. Cao, T. Hou, Comprehensive evaluation of fourteen docking programs on protein-peptide complexes. *J. Chem. Theory Comput.* **16**, 3959–3969 (2020).
43. P. Agrawal, H. Singh, H. K. Srivastava, S. Singh, G. Kishore, G. P. S. Raghava, Benchmarking of different molecular docking methods for protein-peptide docking. *BMC Bioinformatics* **19** (Suppl. 13), 426 (2019).
44. K. B. Santos, I. A. Guedes, A. L. M. Karl, L. E. Dardenne, Highly flexible ligand docking: Benchmarking of the DockThor program on the LEADS-PEP protein-peptide data set. *J. Chem. Inf. Model.* **60**, 667–683 (2020).
45. D. A. Antunes, D. Devaurs, M. Moll, G. Lizée, L. E. Kavraki, General prediction of peptide-MHC binding modes using incremental docking: A proof of concept. *Sci. Rep.* **8**, 4327 (2018).
46. M. Cierny, M. Kurncinski, K. Kamel, A. Kolinski, N. Alam, O. Schueler-Furman, S. Kmiecik, Protein-peptide docking: Opportunities and challenges. *Drug Discov. Today* **23**, 1530–1537 (2018).
47. N. London, B. Raveh, O. Schueler-Furman, Peptide docking and structure-based characterization of peptide binding: From knowledge to know-how. *Curr. Opin. Struct. Biol.* **23**, 894–902 (2013).
48. X. Xu, X. Zou, Predicting protein-peptide complex structures by accounting for peptide flexibility and the physicochemical environment. *J. Chem. Inf. Model.* **62**, 27–39 (2022).
49. V. Apostolopoulos, J. Bojarska, T.-T. Chai, S. Elhagdy, K. Kaczmarek, J. Matsoukas, R. New, K. Parang, O. P. Lopez, H. Parhiz, C. O. Perera, M. Pickholz, M. Remko, M. Saviano, M. Skwarczynski, Y. Tang, W. M. Wolf, T. Yoshiya, J. Zabrocki, P. Zielenkiewicz, M. AlKhazindar, V. Barriga, K. Kelaidonis, E. M. Sarasia, I. Toth, A global review on short peptides: Frontiers and perspectives. *Molecules* **26**, 430 (2021).
50. F. Sievers, D. G. Higgins, Clustal Omega for making accurate alignments of many protein sequences. *Protein Sci.* **27**, 135–145 (2018).
51. D. G. Higgins, J. D. Thompson, T. J. Gibson, Using CLUSTAL for multiple sequence alignments in *Methods in Enzymology* (Academic Press, 1996); (<http://sciencedirect.com/science/article/pii/S0076687996660248>) vol. 266 of *Computer Methods for Macromolecular Sequence Analysis*, pp. 383–402.
52. D. Di Marino, G. Chillemi, S. De Rubeis, A. Tramontano, T. Achsel, C. Bagni, MD and docking studies reveal that the functional switch of CYFIP1 is mediated by a butterfly-like motion. *J. Chem. Theory Comput.* **11**, 3401–3410 (2015).
53. I. D'Annessa, F. S. Di Leva, A. La Teana, E. Novellino, V. Limongelli, D. Di Marino, Bioinformatics and biosimulations as toolbox for peptides and peptidomimetics design: Where are we? *Front. Mol. Biosci.* **7**, 66 (2020).
54. F. S. Di Leva, S. Tomassi, S. Di Maro, F. Reichtart, J. Notni, A. Dangi, U. K. Marelli, D. Brancaccio, F. Merlini, H.-J. Wester, E. Novellino, H. Kessler, L. Marinelli, From a helix to a small cycle: Metadynamics-Inspired $\alpha\beta$ integrin selective ligands. *Angew. Chem. Int. Ed. Engl.* **57**, 14645–14649 (2018).
55. L. Maragliano, E. Vanden-Eijnden, A temperature accelerated method for sampling free energy and determining reaction pathways in rare events simulations. *Chem. Phys. Lett.* **426**, 168–175 (2006).
56. G. Stoltz, E. Vanden-Eijnden, Longtime convergence of the temperature-accelerated molecular dynamics method. *Nonlinearity* **31**, 3748 (2018).
57. A. Lesage, T. Lelièvre, G. Stoltz, J. Hénin, Smoothed biasing forces yield unbiased free energies with the extended-system adaptive biasing force method. *J. Phys. Chem. B* **121**, 3676–3685 (2017).
58. M. Asmari, R. Ratih, H. A. Alhazmi, S. El Deeb, Thermophoresis for characterizing biomolecular interaction. *Methods* **146**, 107–119 (2018).
59. M. Jerabek-Willemsen, T. André, R. Wanner, H. M. Roth, S. Duhr, P. Baaske, D. Breitsprecher, MicroScale thermophoresis: Interaction analysis and beyond. *J. Mol. Struct.* **1077**, 101–113 (2014).
60. T. Inai, The coculture method to examine interactions between claudin isoforms in tight junction-free HEK293 cells and tight junction-bearing MDCK II cells. *Methods Mol. Biol.* **762**, 101–114 (2011).
61. V. Castagnola, L. Deleye, A. Podestà, E. Jaho, F. Loiacono, D. Debelle, M. Trevisani, D. Z. Ciobanu, A. Armirilli, F. Pisani, E. Flahaut, E. Vazquez, M. Bramini, F. Cesca, F. Benfenati, Interactions of graphene oxide and few-layer graphene with the blood-brain barrier. *Nano Lett.* **23**, 2981–2990 (2023).
62. P. J. Gaillard, A. G. de Boer, Relationship between permeability status of the blood-brain barrier and in vitro permeability coefficient of a drug. *Eur. J. Pharm. Sci.* **12**, 95–102 (2000).
63. T. S. Frost, L. Jiang, Y. Zohar, Pharmacokinetic analysis of epithelial/endothelial cell barriers in microfluidic bilayer devices with an air-liquid interface. *Micromachines* **11**, 536 (2020).
64. N. Shashikanth, M. M. France, R. Xiao, X. Haest, H. E. Rizzo, J. Yeste, J. Reiner, J. R. Turner, Tight junction channel regulation by interclaudin interference. *Nat. Commun.* **13**, 3780 (2022).
65. A. Hartsock, W. J. Nelson, Adherens and tight junctions: Structure, function and connections to the actin cytoskeleton. *Biochim. Biophys. Acta* **1778**, 660–669 (2008).
66. H. K. Campbell, J. L. Maiers, K. A. DeMali, Interplay between tight junctions & adherens junctions. *Exp. Cell Res.* **358**, 39–44 (2017).
67. G. Del Vecchio, C. Tscheik, K. Tenz, H. C. Helms, L. Winkler, R. Blasig, I. E. Blasig, Sodium caprate transiently opens Claudin-5-containing barriers at tight junctions of epithelial and endothelial cells. *Mol. Pharm.* **9**, 2523–2533 (2012).
68. S. M. Krug, M. Amasheh, I. Dittmann, I. Christoffel, M. Fromm, S. Amasheh, Sodium caprate as an enhancer of macromolecule permeation across tricellular tight junctions of intestinal cells. *Biomaterials* **34**, 275–282 (2013).
69. Y. Hashimoto, W. Zhou, K. Hamachi, K. Shirakura, T. Doi, K. Yagi, T. Sawasaki, Y. Okada, M. Kondoh, H. Takeda, Engineered membrane protein antigens successfully induce antibodies against extracellular regions of claudin-5. *Sci. Rep.* **8**, 8383 (2018).
70. K. Tachibana, Y. Hashimoto, K. Shirakura, Y. Okada, R. Hirayama, Y. Iwashita, I. Nishino, Y. Ago, H. Takeda, H. Kuniyasu, M. Kondoh, Safety and efficacy of an anti-claudin-5 monoclonal antibody to increase blood-brain barrier permeability for drug delivery to the brain in a non-human primate. *J. Control. Release* **336**, 105–111 (2021).
71. R. I. Mehta, J. S. Carpenter, R. I. Mehta, M. W. Haut, P. Wang, M. Ranjan, U. Najib, P.-F. D'Haese, A. R. Rezai, Ultrasound-mediated blood-brain barrier opening uncovers an intracerebral perivenous fluid network in persons with Alzheimer's disease. *Fluids Barriers CNS* **20**, 46 (2023).
72. M. Cavaco, J. Valle, I. Flores, D. Andreu, M. A. R. B. Castanho, Estimating peptide half-life in serum from tunable, sequence-related physicochemical properties. *Clin. Transl. Sci.* **14**, 1349–1358 (2021).
73. S. Dabrowski, C. Staats, D. Zwanziger, R.-S. Sauer, C. Bellmann, R. Günther, E. Krause, R. F. Haseloff, H. Rittner, I. E. Blasig, Redox-sensitive structure and function of the first extracellular loop of the cell-cell contact protein Claudin-1: lessons from molecular structure to animals. *Antioxid. Redox Signal.* **22**, 1–14 (2015).

74. Y. Saitoh, H. Suzuki, K. Tani, K. Nishikawa, K. Irie, Y. Ogura, A. Tamura, S. Tsukita, Y. Fujiyoshi, Tight junctions. Structural insight into tight junction disassembly by Clostridium perfringens enterotoxin. *Science* **347**, 775–778 (2015).
75. Y. Hashimoto, M. Campbell, K. Tachibana, Y. Okada, M. Kondoh, Claudin-5: A pharmacological target to modify the permeability of the blood–brain barrier. *Biol. Pharm. Bull.* **44**, 1380–1390 (2021).
76. S. M. Stamatovic, R. F. Keep, M. M. Wang, I. Jankovic, A. V. Andjelkovic, Caveolae-mediated Internalization of Occludin and Claudin-5 during CCL2-induced tight junction remodeling in brain endothelial cells. *J. Biol. Chem.* **284**, 19053–19066 (2009).
77. S. M. Stamatovic, R. F. Keep, A. V. Andjelkovic, Tracing the endocytosis of claudin-5 in brain endothelial cells. *Methods Mol. Biol.* **762**, 303–320 (2011).
78. D. Zwanziger, C. Staat, A. V. Andjelkovic, I. E. Blasig, Claudin-derived peptides are internalized via specific endocytosis pathways. *Ann. N. Y. Acad. Sci.* **1257**, 29–37 (2012).
79. N. Beeman, P. G. Webb, H. K. Baumgartner, Occludin is required for apoptosis when claudin–claudin interactions are disrupted. *Cell Death Dis.* **3**, e273–e273 (2012).
80. B. Schlingmann, C. E. Overgaard, S. A. Molina, K. S. Lynn, L. A. Mitchell, S. Dorsainvil White, A. L. Mattheyses, D. M. Guidot, C. T. Capaldo, M. Koval, Regulation of claudin/zonula occludens-1 complexes by hetero-claudin interactions. *Nat. Commun.* **7**, 12276 (2016).
81. M. Campbell, F. Hanrahan, O. L. Gobbo, M. E. Kelly, A.-S. Kiang, M. M. Humphries, A. T. H. Nguyen, E. Ozaki, J. Keaney, C. W. Blau, C. M. Kerskens, S. D. Cahalan, J. J. Callanan, E. Wallace, G. A. Grant, C. P. Doherty, P. Humphries, Targeted suppression of claudin-5 decreases cerebral oedema and improves cognitive outcome following traumatic brain injury. *Nat. Commun.* **3**, 849 (2012).
82. T. Nitta, M. Hata, S. Gotoh, Y. Seo, H. Sasaki, N. Hashimoto, M. Furuse, S. Tsukita, Size-selective loosening of the blood-brain barrier in claudin-5-deficient mice. *J. Cell Biol.* **161**, 653–660 (2003).
83. M. Campbell, A.-S. Kiang, P. F. Kenna, C. Kerskens, C. Blau, L. O'Dwyer, A. Tivnan, J. A. Kelly, B. Brankin, G.-J. Farrar, P. Humphries, RNAi-mediated reversible opening of the blood-brain barrier. *J. Gene Med.* **10**, 930–947 (2008).
84. S. E. Feller, Y. Zhang, R. W. Pastor, B. R. Brooks, Constant pressure molecular dynamics simulation: The Langevin piston method. *J. Chem. Phys.* **103**, 4613–4621 (1995).
85. G. J. Martyna, D. J. Tobias, M. L. Klein, Constant pressure molecular dynamics algorithms. *J. Chem. Phys.* **101**, 4177–4189 (1994).
86. J. Huang, S. Rauscher, G. Nawrocki, T. Ran, M. Feig, B. L. de Groot, H. Grubmüller, A. D. MacKerell Jr., CHARMM36m: An improved force field for folded and intrinsically disordered proteins. *Nat. Methods* **14**, 71–73 (2017).
87. J. C. Phillips, D. J. Hardy, J. D. C. Maia, J. E. Stone, J. V. Ribeiro, R. C. Bernardi, R. Buch, G. Fiorin, J. Hénin, W. Jiang, R. McGreevy, M. C. R. Melo, B. K. Radak, R. D. Skeel, A. Singhary, Y. Wang, B. Roux, A. Aksimentiev, Z. Luthey-Schulten, L. V. Kalé, K. Schulten, C. Chipot, E. Tajkhorshid, Scalable molecular dynamics on CPU and GPU architectures with NAMD. *J. Chem. Phys.* **153**, 044130 (2020).
88. Y. Kuroda, A. Suenaga, Y. Sato, S. Kosuda, M. Taiji, All-atom molecular dynamics analysis of multi-peptide systems reproduces peptide solubility in line with experimental observations. *Sci. Rep.* **6**, 19479 (2016).
89. J. B. Klauda, R. M. Venable, J. A. Freites, J. W. O'Connor, D. J. Tobias, C. Mondragon-Ramirez, I. Vorobyov, A. D. MacKerell, R. W. Pastor, Update of the CHARMM all-atom additive force field for lipids: Validation on six lipid types. *J. Phys. Chem. B* **114**, 7830–7843 (2010).
90. W. Humphrey, A. Dalke, K. Schulten, VMD: Visual molecular dynamics. *J. Mol. Graph.* **14**, 27–28 (1996).
91. M. Lapelosa, Conformational dynamics and free energy of BHFR1 binding to Bim BH3. *Biophys. Chem.* **232**, 22–28 (2018).
92. G. Fiorin, A. Pastore, P. Carloni, M. Parrinello, Using metadynamics to understand the mechanism of calmodulin/target recognition at atomic detail. *Biophys. J.* **91**, 2768–2777 (2006).
93. S. Wingbermühle, L. V. Schäfer, Capturing the flexibility of a protein–ligand complex: Binding free energies from different enhanced sampling techniques. *J. Chem. Theory Comput.* **16**, 4615–4630 (2020).
94. G. Lamothe, T. E. Malliavin, re-TAMD: Exploring interactions between H3 peptide and YEATS domain using enhanced sampling. *BMC Struct. Biol.* **18**, 4 (2018).
95. C. Abrams, G. Bussi, Enhanced sampling in molecular dynamics using metadynamics, replica-exchange, and temperature-acceleration. *Entropy* **16**, 163–199 (2014).
96. G. M. Torrie, J. P. Valleau, Nonphysical sampling distributions in Monte Carlo free-energy estimation: Umbrella sampling. *J. Comput. Phys.* **23**, 187–199 (1977).
97. H. Fu, X. Shao, C. Chipot, W. Cai, Extended adaptive biasing force algorithm. An on-the-fly implementation for accurate free-energy calculations. *J. Chem. Theory Comput.* **12**, 3506–3513 (2016).
98. J. Comer, J. C. Gumbart, J. Hénin, T. Lelièvre, A. Pohorille, C. Chipot, The adaptive biasing force method: Everything you always wanted to know but were afraid to ask. *J. Phys. Chem. B* **119**, 1129–1151 (2015).
99. V. Limongelli, M. Bonomi, M. Parrinello, Funnel metadynamics as accurate binding free-energy method. *Proc. Natl. Acad. Sci. U.S.A.* **110**, 6358–6363 (2013).
100. M. Lapelosa, Free energy of binding and mechanism of interaction for the MEEVD-TPR2A peptide–protein complex. *J. Chem. Theory Comput.* **13**, 4514–4523 (2017).
101. H.-J. Woo, B. Roux, Calculation of absolute protein-ligand binding free energy from computer simulations. *Proc. Natl. Acad. Sci. U.S.A.* **102**, 6825–6830 (2005).
102. Y. Deng, B. Roux, Computations of standard binding free energies with molecular dynamics simulations. *J. Phys. Chem. B* **113**, 2234–2246 (2009).
103. M. Blazhynska, E. G. C. de Lacam, H. Chen, B. Roux, C. Chipot, Hazardous shortcuts in standard binding free energy calculations. *J. Phys. Chem. Lett.* **13**, 6250–6258 (2022).
104. V. Limongelli, Ligand binding free energy and kinetics calculation in 2020. *WIREs Comput. Mol. Sci.* **10**, (2020).
105. L. Maragliano, E. Vanden-Eijnden, Single-sweep methods for free energy calculations. *J. Chem. Phys.* **128**, 184110 (2008).
106. L. Maragliano, G. Cottone, G. Cicotti, E. Vanden-Eijnden, Mapping the network of pathways for CO diffusion in myoglobin. *J. Am. Chem. Soc.* **132**, 1010–1017 (2010).
107. C. F. Abrams, E. Vanden-Eijnden, On-the-fly free energy parameterization via temperature accelerated molecular dynamics. *Chem. Phys. Lett.* **547**, 114–119 (2012).
108. G. Alberini, S. Alexis Paz, B. Corradi, C. F. Abrams, F. Benfenati, L. Maragliano, Molecular dynamics simulations of ion permeation in human voltage-gated sodium channels. *J. Chem. Theory Comput.* **19**, 2953–2972 (2023).
109. G. Fiorin, M. L. Klein, J. Hénin, Using collective variables to drive molecular dynamics simulations. *Mol. Phys.* **111**, 3345–3362 (2013).
110. H. Chen, H. Fu, X. Shao, C. Chipot, W. Cai, ELF: An extended-lagrangian free energy calculation module for multiple molecular dynamics engines. *J. Chem. Inf. Model.* **58**, 1315–1318 (2018).
111. G. Wang, X. Li, Z. Wang, APD3: The antimicrobial peptide database as a tool for research and education. *Nucleic Acids Res.* **44**, D1087–D1093 (2016).
112. J. Zhang, Y. Liang, Y. Zhang, Atomic-level protein structure refinement using fragment-guided molecular dynamics conformation sampling. *Structure* **19**, 1784–1795 (2011).
113. E. Gasteiger, C. Hoogland, A. Gattiker, S. Duvaud, M. R. Wilkins, R. D. Appel, A. Bairoch, Protein Identification and Analysis Tools on the ExPASy Server in *The Proteomics Protocols Handbook*, J. M. Walker, Ed. (Humana Press, 2005); (<https://doi.org/10.1385/1-59259-890-0:571>) *Springer Protocols Handbooks*, pp. 571–607.
114. A. Waterhouse, M. Bertoni, S. Bienert, G. Studer, G. Tauriello, R. Gumienny, F. T. Heer, T. A. P. de Beer, C. Rempp, L. Bordoli, R. Lepore, T. Schwede, SWISS-MODEL: Homology modelling of protein structures and complexes. *Nucleic Acids Res.* **46**, W296–W303 (2018).
115. N. Hurwitz, D. Schneidman-Duhovny, H. J. Wolfson, Memdock: An α -helical membrane protein docking algorithm. *Bioinformatics* **32**, 2444–2450 (2016).
116. L. Heo, H. Lee, C. Seok, GalaxyRefineComplex: Refinement of protein-protein complex model structures driven by interface repacking. *Sci. Rep.* **6**, 32153 (2016).
117. A. Lamiable, P. Thévenet, J. Rey, M. Vavrusa, P. Derreumaux, P. Tufféry, PEP-FOLD3: Faster de novo structure prediction for linear peptides in solution and in complex. *Nucleic Acids Res.* **44**, W449–W454 (2016).
118. W. C. Still, A. Tempczyk, R. C. Hawley, T. Hendrickson, Semianalytical treatment of solvation for molecular mechanics and dynamics. *J. Am. Chem. Soc.* **112**, 6127–6129 (1990).
119. R. Constandiel, R. Contreras, Self consistent field theory of solvent effects representation by continuum models: Introduction of desolvation contribution. *Theoret. Chim. Acta* **65**, 1–11 (1984).
120. W. L. Jorgensen, J. Chandrasekhar, J. D. Madura, R. W. Impey, M. L. Klein, Comparison of simple potential functions for simulating liquid water. *J. Chem. Phys.* **79**, 926–935 (1983).
121. S. Jo, T. Kim, V. G. Iyer, W. Im, CHARMM-GUI: A web-based graphical user interface for CHARMM. *J. Comput. Chem.* **29**, 1859–1865 (2008).
122. T. Darden, D. York, L. Pedersen, Particle mesh Ewald: An $N\log(N)$ method for Ewald sums in large systems. *J. Chem. Phys.* **98**, 10089–10092 (1993).
123. P. J. Steinbach, B. R. Brooks, New spherical-cutoff methods for long-range forces in macromolecular simulation. *J. Comput. Chem.* **15**, 667–683 (1994).
124. J.-P. Ryckaert, G. Cicotti, H. J. C. Berendsen, Numerical integration of the cartesian equations of motion of a system with constraints: Molecular dynamics of n-alkanes. *J. Comput. Phys.* **23**, 327–341 (1977).
125. S. Miyamoto, P. A. Kollman, SETTLE: An analytical version of the SHAKE and RATTLE algorithm for rigid water models. *J. Comput. Chem.* **13**, 952–962 (1992).
126. D. Xu, Y. Zhang, Improving the physical realism and structural accuracy of protein models by a two-step atomic-level energy minimization. *Biophys. J.* **101**, 2525–2534 (2011).
127. S. Jo, X. Cheng, S. M. Islam, L. Huang, H. Rui, A. Zhu, H. S. Lee, Y. Qi, W. Han, K. Vanommeslaeghe, A. D. MacKerell, B. Roux, W. Im, CHARMM-GUI PDB manipulator for advanced modeling and simulations of proteins containing nonstandard residues. *Adv. Protein Chem. Struct. Biol.* **96**, 235–265 (2014).
128. O. Trott, A. J. Olson, AutoDock Vina: Improving the speed and accuracy of docking with a new scoring function, efficient optimization, and multithreading. *J. Comput. Chem.* **31**, 455–461 (2010).

129. D. S. Goodsell, M. F. Sanner, A. J. Olson, S. Forli, The AutoDock suite at 30. *Protein Sci.* **30**, 31–43 (2021).
130. G. M. Morris, R. Huey, W. Lindstrom, M. F. Sanner, R. K. Belew, D. S. Goodsell, A. J. Olson, AutoDock4 and AutoDockTools4: Automated docking with selective receptor flexibility. *J. Comput. Chem.* **30**, 2785–2791 (2009).
131. E. F. Pettersen, T. D. Goddard, C. C. Huang, G. S. Couch, D. M. Greenblatt, E. C. Meng, T. E. Ferrin, UCSF Chimera—a visualization system for exploratory research and analysis. *J. Comput. Chem.* **25**, 1605–1612 (2004).
132. N. London, B. Raveh, E. Cohen, G. Fathi, O. Schueler-Furman, Rosetta FlexPepDock web server—high resolution modeling of peptide–protein interactions. *Nucleic Acids Res.* **39**, W249–W253 (2011).
133. N. Alam, O. Schueler-Furman, Modeling peptide–protein structure and binding using Monte Carlo sampling approaches: Rosetta FlexPepDock and FlexPepBind. *Methods Mol. Biol.* **1561**, 139–169 (2017).
134. R. Rentzsch, B. Y. Renard, Docking small peptides remains a great challenge: An assessment using AutoDock Vina. *Brief. Bioinform.* **16**, 1045–1056 (2015).
135. S. Y. Noskov, B. Roux, Control of ion selectivity in LeuT: Two Na^+ binding sites with two different mechanisms. *J. Mol. Biol.* **377**, 804–818 (2008).
136. Y. Luo, B. Roux, Simulation of osmotic pressure in concentrated aqueous salt solutions. *J. Phys. Chem. Lett.* **1**, 183–189 (2010).
137. R. M. Venable, Y. Luo, K. Gawrisch, B. Roux, R. W. Pastor, Simulations of anionic lipid membranes: Development of interaction-specific ion parameters and validation using NMR data. *J. Phys. Chem. B* **117**, 10183–10192 (2013).
138. T. W. Allen, O. S. Andersen, B. Roux, Energetics of ion conduction through the gramicidin channel. *Proc. Natl. Acad. Sci. U.S.A.* **101**, 117–122 (2004).
139. B. Roux, O. S. Andersen, T. W. Allen, Comment on “Free energy simulations of single and double ion occupancy in gramicidin A” [J. Chem. Phys. 126, 105103 (2007)]. *J. Chem. Phys.* **128**, 227101 (2008).
140. J. C. Gumbart, B. Roux, C. Chipot, Standard binding free energies from computer simulations: What is the best strategy? *J. Chem. Theory Comput.* **9**, 794–802 (2013).
141. J. C. Gumbart, B. Roux, C. Chipot, Efficient determination of protein–protein standard binding free energies from first principles. *J. Chem. Theory Comput.* **9**, 3789–3798 (2013).
142. H. Fu, W. Cai, J. Hénin, B. Roux, C. Chipot, New coarse variables for the accurate determination of standard binding free energies. *J. Chem. Theory Comput.* **13**, 5173–5178 (2017).
143. H. Fu, H. Chen, M. Blazhynska, E. G. C. de Lacam, F. Szczepaniak, A. Pavlova, X. Shao, J. C. Gumbart, F. Dehez, B. Roux, W. Cai, C. Chipot, Accurate determination of protein:ligand standard binding free energies from molecular dynamics simulations. *Nat. Protoc.* **17**, 1114–1141 (2022).
144. J. Lan, J. Ge, J. Yu, S. Shan, H. Zhou, S. Fan, Q. Zhang, X. Shi, Q. Wang, L. Zhang, X. Wang, Structure of the SARS-CoV-2 spike receptor-binding domain bound to the ACE2 receptor. *Nature* **581**, 215–220 (2020).
145. S. Doudou, N. A. Burton, R. H. Henchman, Standard free energy of binding from a one-dimensional potential of mean force. *J. Chem. Theory Comput.* **5**, 909–918 (2009).

Acknowledgments: We thank A. Vignolo and M. Pini for the assistance at Fondazione Istituto Italiano di Tecnologia (IIT) computing center. Moreover, we are grateful to S. Decherchi for assistance with the IIT computing center and useful discussions about machine learning. We also mention D. Moruzzo, I. Dallorto, R. Ciancio, and A. Mehilli for administrative assistance and technical help. We also acknowledge the HPC infrastructure and the Support Team at Fondazione Istituto Italiano di Tecnologia. **Funding:** The project has received funding from Telethon-Italy (grant Glut1 to F.Z. and F.B.), the European Union’s Horizon 2020 Research and Innovation Programme under grant agreement no. 881603 Graphene Flagship Core 3 (to F.B.), the Italian Ministry of Health (Ricerca Finalizzata GR-2021-12372966 to V.Cas.), and IRCCS Ospedale Policlinico San Martino, Genova, Italy (Ricerca Corrente and “5x1000” to F.B. and V.Cas.). We acknowledge the CINECA award under the ISCRA initiative (project IsB27, ID: HP10BQDIDT, granted to L.M. and project IsCa5, ID: HP10CQUP2X granted to A.B.).

Author contributions: Authors’ contributions are attributed on the basis of CRedit author statement. M.T.: Conceptualization, investigation, methodology, resources, validation, data curation, formal analysis, visualization, writing—original draft, and writing—review and editing. A.B.: Conceptualization, investigation, methodology, validation, formal analysis, software, data curation, project administration, visualization, writing—original draft, and writing—review and editing. G.A.: Conceptualization, investigation, methodology, validation, formal analysis, writing—original draft, supervision, and project administration. E.C.: Conceptualization, investigation, methodology, validation, and formal analysis. S.V.: Resources, formal analysis, software, visualization, and validation. V. Car: Conceptualization, investigation and formal analysis. E.M.: Investigation and resources. D.Z.C.: Investigation, validation, and data curation. C.B.: Investigation, validation, and data curation. A.A.: Investigation and formal analysis. F.P.: Methodology. F.Z.: Conceptualization, project administration, funding acquisition, and supervision. V. Cas: Conceptualization, investigation, methodology, validation, formal analysis, project administration, visualization, writing—original draft, supervision, and funding acquisition. L.M.: Conceptualization, methodology, writing—review and editing, resources, data curation, validation, supervision, formal analysis, software, project administration, and visualization. F.B.: Conceptualization, supervision, writing—review and editing, validation, methodology, formal analysis, project administration, resources, and funding acquisition.

Competing interests: The authors declare that they have no competing interests. **Data and materials availability:** All data needed to evaluate the conclusions in the paper are present in the paper and/or the Supplementary Materials. Structures, input files, analysis scripts for MD simulations, confocal images, and raw data for MST, TEER, barrier translocation, and Western blot are available at <https://zenodo.org/records/13918544>.

Submitted 5 May 2024

Accepted 9 December 2024

Published 10 January 2025

10.1126/sciadv.adq2616